

To bin or not to bin: analyzing single-cell growth data

Prathitha Kar^{1,2}, Sriram Tiruvadi-Krishnan³, Jaana Männik³, Jaan Männik*³,
and Ariel Amir^{†1}

¹*School of Engineering and Applied Sciences, Harvard University, Cambridge, MA 02134, USA*

²*Department of Chemistry and Chemical Biology, Harvard University, Cambridge, MA 02138, USA*

³*Department of Physics and Astronomy, University of Tennessee, Knoxville, TN 37996, USA*

*Corresponding author- email: jmannik@utk.edu; phone: +1 (865) 974 6018

†Corresponding author- email: arielamir@seas.harvard.edu; phone: +1 (617) 495 5818

11 Abstract

12 Collection of high-throughput data has become prevalent in biology. Large datasets allow
13 the use of statistical constructs such as binning and linear regression to quantify relationships
14 between variables and hypothesize underlying biological mechanisms based on it. We discuss
15 several such examples in relation to single-cell data and cellular growth. In particular, we
16 show instances where what appears to be ordinary use of these statistical methods leads
17 to incorrect conclusions such as growth being non-exponential as opposed to exponential
18 and vice versa. We propose that the data analysis and its interpretation should be done in
19 the context of a generative model, if possible. In this way, the statistical methods can be
20 validated either analytically or against synthetic data generated via the use of the model,
21 leading to a consistent method for inferring biological mechanisms from data. On applying
22 the validated methods of data analysis to infer cellular growth on our experimental data, we
23 find the growth of length in *E. coli* to be non-exponential. Our analysis shows that in the
24 later stages of the cell cycle the growth rate is faster than exponential.

25 1 Introduction

26 The last decade has seen a tremendous increase in the availability of high-quality large
27 datasets in biology, in particular in the context of single-cell level measurements. Such data
28 are complementary to “bulk” measurements made over a population of cells. They have
29 led to new biological paradigms and motivated the development of quantitative models [1–
30 7]. Nevertheless, they have also led to new challenges in data analysis, and here we will
31 point out some of the pitfalls that exist in handling such data. In particular, we will show
32 that the commonly used procedure of binning data in order to eliminate noise (averaging
33 conditioned on the value of one of the variables) may lead to smooth curves that hint at
34 specific functional relations between the two variables plotted that are inconsistent with
35 the true functional relations. As we shall show, this may come about due to the “hidden”
36 noise sources that affect the binning procedure and the phenomenon of “inspection bias”
37 where certain bins have biased contributions. One of our main take home messages is the
38 significance of having an underlying model (or models) to guide/test/validate data analysis
39 methods. The underlying model is referred to as a generative model in the sense that
40 it leads to similar data to that observed in the experiments. The importance of a so-
41 called generative model has been beautifully advocated in the context of astrophysical data
42 analysis [8], yet biology brings in a plethora of exciting differences: while in physics noise from
43 measurement instruments often dominates, in the biological examples we will dwell on here it
44 is the *intrinsic* biological noise that can obscure the mathematical relation between variables
45 when not handled properly. In the following, we will illustrate this rather philosophical
46 introduction on a concrete and fundamental example, albeit *e pluribus unum*. We will focus
47 on the analysis of the *Escherichia coli* growth curves obtained via high throughput optical
48 microscopy. Nevertheless we anticipate the conceptual points made here – and demonstrated
49 on a particular example of interest – will translate to other types of measurements, which

50 make use of microscopy but also beyond.

51 Binning corresponds to grouping data based on the value of the x-axis variable, and find-
52 ing the mean of the fluctuating y-axis variable for this group. By removing the fluctuations
53 of the y-variable, the binning process often aims to expose the “true” functional relation
54 between the two variables which can be used to infer the underlying biological mechanism.
55 It is important to discuss the sources of fluctuations in the y-axis variable before we proceed.
56 In biology, fluctuations in the variables arise inevitably from the intrinsic variability within
57 a cell population. Cells growing in the same medium and environment have different charac-
58 teristics (e.g., growth rate) due to the stochastic nature of biochemical reactions in the cell
59 [9]. For example, the division event is controlled by stochastic reactions, whose variability
60 leads to cell dividing at a size smaller or larger than the mean. In this paper, when modeling
61 the data, we will consider the intrinsic noise as the only source of variability and assume
62 that the measurement error is much smaller than the intrinsic variation in the population.

63 One example of the use of binning is shown in Figure 1A where size at division (L_d) vs
64 size at birth (L_b) is plotted using experimental data obtained by Tanouchi *et al.* for *E. coli*
65 growing at 25°C [10]. In Figure 1A, the functional relation between length at division and
66 length at birth for *E. coli* is observed to be linear and close to $L_d = L_b + \Delta L$ (see Section 5.11.1
67 for details). The relation obtained allows us to hypothesize a coarse-grained biological model
68 known as the adder model as shown in Figure 1B in which the length at division is set by
69 addition of length ΔL from birth [4, 11–16]. This example demonstrates the use of statistical
70 analysis on single-cell data to understand the underlying cell regulation mechanisms. Using
71 statistical methods such as binning and linear regression, other phenomenological models
72 apart from adder have also been proposed in *E. coli* where the division length (L_d) is not
73 directly “set” by that at birth [17–19]. The phenomenological models, in turn, can be related
74 to mechanistic (molecular-level) models of cell size and cell cycle regulation [20]. Recent
75 work has shed light on the subtleties involved in interpreting the linear regression results for

76 the L_d vs L_b plot where seemingly adder behavior in length can be obtained from a sizer
77 model (division occurring on reaching a critical size) due to the interplay of multiple sources
78 of variability [21]. This issue is similar in spirit to those we highlight here.

79 The volume growth of single bacterial cells has been typically assumed to be exponential
80 [4, 14, 22–25]. Assuming ribosomes to be the limiting component in translation, growth is
81 predicted to be exponential and growth rate depends on the active ribosome content in the
82 cell [26–28]. Under the assumption of exponential growth, the size at birth (L_b), the size at
83 division (L_d), and the generation time (T_d) are related to each other by,

$$\ln\left(\frac{L_d}{L_b}\right) = \lambda T_d, \quad (1)$$

84 where λ is the growth rate. Understanding the mode of growth is important e.g., due to
85 its potential effects on cell size homeostasis. Exponentially growing cells cannot employ a
86 mechanism where they control division by timing a constant duration from birth but such
87 a mechanism is possible in case of linear growth [3, 13, 29]. Linear regression performed
88 on $\ln\left(\frac{L_d}{L_b}\right)$ vs $\langle \lambda \rangle T_d$ plot, where $\langle \lambda \rangle$ is the mean growth rate, was used to infer the mode
89 of growth in the archaeon *H. salinarum* [16], and in the bacteria *M. smegmatis* [30] and
90 *C. glutamicum* [31], for example. If the best linear fit follows the $y=x$ trend, the resulting
91 functional relation might point to growth being exponential. A corollary to this is the
92 rejection of exponential growth when the slope and intercept of the best linear fit deviate from
93 one and zero respectively [31]. Thus, binning and linear regression applied on single-cell data
94 appear to provide information about the underlying biology, in this case, the mode of cellular
95 growth. We will test the validity of such inference by analyzing synthetic data generated
96 using generative models. We find that linear regression performed on the plot $\ln\left(\frac{L_d}{L_b}\right)$ vs
97 $\langle \lambda \rangle T_d$, surprisingly, does not provide information about the mode of growth. Nonetheless,
98 we show that other methods of statistical analysis such as binning growth rate vs age plots

99 are adequate in addressing the problem. Using these validated methods on experimental
100 data, we find that *E. coli* grows non-exponentially. In later stages of the cell cycle, the
101 growth rate is higher than that in early stages.

102 2 Statistical methods like binning and linear regression 103 should be interpreted based on a model.

104 To illustrate the pitfalls associated with binning, we use data from recent experiments on *E.*
105 *coli* where the length at birth, the length at division and the generation time were obtained
106 for multiple cells (see Section 5.1 and [32]). Phase-contrast microscopy was used to obtain
107 cell length at equal intervals of time. Note that we consider length as a proxy for cell size as
108 the fluctuations in the width of *E. coli* cells are negligible in a given condition [15, 23, 33, 34].

109 To investigate if the cell growth was exponential, we plotted $\ln(\frac{L_d}{L_b})$ vs $\langle \lambda \rangle T_d$ for cells growing
110 in M9 alanine minimal medium at 28°C ($\langle T_d \rangle = 214$ min). The linear regression of these
111 data yields a slope of 0.3 and an intercept of 0.4 as shown in Figure 2A. The binned data and
112 the best linear fit deviate significantly from the y=x line (see Table S2). Additionally, the
113 binned data follows a non-linear trend and flattens out at longer generation times. We also
114 found similar deviations in the binned data and best linear fit in glycerol medium ($\langle T_d \rangle =$
115 164 min) shown in Figure 2- figure supplement 1A, and glucose-cas medium ($\langle T_d \rangle = 65$ min)
116 shown in Figure 2- figure supplement 1B. Qualitatively similar results have been recently
117 obtained for another bacterium, *C. glutamicum*, in Ref. [31]. These results might point to
118 growth being non-exponential.

119 Next we will approach the same problem but with a generative model. We will first
120 show that the aforementioned non-linear dependencies are perfectly consistent with purely
121 exponential growth. For the model, we consider exponential growth where the growth rate
122 is distributed normally and independently between cell cycles with mean growth rate $\langle \lambda \rangle$

123 and standard deviation $CV_\lambda \langle \lambda \rangle$. CV_λ is thus the coefficient of variation (CV) of the growth
 124 rate and is assumed to be small. To maintain a narrow distribution of cell size, cells must
 125 employ regulatory mechanisms. In our model, we assume that, barring the noise due to
 126 stochastic biochemical reactions, cells attempt to divide at a particular size L_d given size at
 127 birth L_b . Keeping the model as generic as possible, we can write L_d as a function of L_b , $f(L_b)$
 128 which can be thought of as a coarse-grained model for the regulatory mechanism. Ref. [13]
 129 provides a framework to capture the regulatory mechanisms by choosing $f(L_b) = 2L_b^{1-\alpha}L_0^\alpha$.
 130 L_0 is the typical size at birth and α , which can take values between 0 and 2, reflects the
 131 strength of regulation strategy. $\alpha = 0$ corresponds to the timer model where division occurs
 132 on average after a constant time from birth, and $\alpha = 1$ is the sizer model where a cell divides
 133 upon reaching a critical size. $\alpha = 1/2$ can be shown to be equivalent to the adder model
 134 where division is controlled by addition of constant size from birth [13]. In addition to the
 135 deterministic function (f) specifying division, the size at division is affected by noise ($\frac{\zeta}{\langle \lambda \rangle}$)
 136 in division timing. We assume it has a Gaussian distribution with mean zero and standard
 137 deviation $\frac{\sigma_n}{\langle \lambda \rangle}$ and that it is independent of the growth rate. Thus, the generation time (T_d)
 138 can be mathematically written as $T_d = \frac{1}{\lambda} \ln\left(\frac{f(L_b)}{L_b}\right) + \frac{\zeta}{\langle \lambda \rangle}$ and is influenced by growth rate noise
 139 and division timing noise. Note that replacing the time additive division timing noise with
 140 a size additive division timing noise will not affect the results qualitatively (see Sections 5.2
 141 and 5.3 for details and Table S1 for variable definitions).

142 For perfectly symmetrically dividing cells whose sizes are narrowly distributed, the trend
 143 in the binned data for $\ln\left(\frac{L_d}{L_b}\right)$ vs $\langle \lambda \rangle T_d$ plot is found to be (see Section 5.4),

$$y = x \left(1 + \frac{1 - \frac{x}{\ln(2)}}{1 + \frac{2}{2-\alpha} \frac{\sigma_n^2}{CV_\lambda^2 \ln^2(2)}} \right). \quad (2)$$

144 Fixing $CV_\lambda = \sigma_n = 0.15$, we show using simulations in Figure 2C the non-linear trend in the
 145 binned data even though we assumed exponential growth. Similarly, on performing linear

146 regression on $\ln(\frac{L_d}{L_b})$ vs $\langle \lambda \rangle T_d$ plot, we find that the slope is not equal to one and the intercept
147 is non-zero (see Eqs. 27 and 28). Eq. 2 shows that the trend in the binned data depends
148 on the ratio of growth rate noise and division timing noise. The slope is equal to one and
149 intercept is zero only if the noise in growth rate is negligible. In experiments that is rarely
150 the case, hence, the binned data trend and the best linear fit deviate from the y=x line
151 even though growth might be exponential. Thus, we cannot rule out exponential growth in
152 the *E. coli* experiments despite the binned data trend being non-linear and the best-fit line
153 deviating from the y=x line.

154 Why does a non-linear relationship in the binned data for the plot $\ln(\frac{L_d}{L_b})$ vs $\langle \lambda \rangle T_d$ arise
155 even for exponential growth? According to the model, L_d is determined by a deterministic
156 strategy, $f(L_b)$ and a time/size additive division timing noise. The noise component which
157 affects L_d and subsequently the quantity $\ln(\frac{L_d}{L_b})$ is thus the noise in division timing and not
158 the growth rate. The generation time (T_d) plotted on the x-axis is influenced by the noise in
159 division timing as well as the noise in growth rate. Binning assumes that for a fixed value of
160 the x-axis variable, the noise from other sources affects only the y-axis variable (the binned
161 variable). Similarly for linear regression, the underlying assumption is that the independent
162 variable on x-axis is precisely known while the dependent variable on the y-axis is influenced
163 by the independent variable and from external factors other than the independent variable.
164 In this case, only $\langle \lambda \rangle T_d$ plotted on x-axis is influenced by growth rate noise while both $\langle \lambda \rangle T_d$
165 and $\ln(\frac{L_d}{L_b})$ are influenced by noise in division time. This does not fit the assumption for
166 binning and linear regression and hence, the best linear fit for $\ln(\frac{L_d}{L_b})$ vs $\langle \lambda \rangle T_d$ plot might
167 deviate from the y=x line even in the case of exponential growth.

168 Another way of explaining the deviation from the linear y=x trend is by inspection bias,
169 which arises when certain data is over-represented [35]. Cells which have a longer generation
170 time than the mean will most likely have a slower growth rate. Thus, in Figure 2A and
171 Figure 2C, at larger values of $\langle \lambda \rangle T_d$ or T_d , the bin averages are biased by slower growing

172 cells, thus making $\ln(\frac{L_d}{L_b})$ or λT_d to be lower than expected. This provides an explanation
173 for the flattening of the trend.

174 It follows from the previous discussion that if one bins data by $\ln(\frac{L_d}{L_b})$ then the assumption
175 for binning is met. Both of the variables $\langle \lambda \rangle T_d$ and $\ln(\frac{L_d}{L_b})$ are influenced by the noise in
176 division time but $\langle \lambda \rangle T_d$ plotted on the y-axis is also influenced by the growth rate noise.
177 Thus, the y-axis variable, $\langle \lambda \rangle T_d$ is determined by the x-axis variable, $\ln(\frac{L_d}{L_b})$, and an external
178 source of noise, in this case, the growth rate noise. Thus, based on our model, we expect the
179 trend in binned data and linear regression performed on the interchanged axes to follow the
180 y=x trend for exponentially growing cells (see Section 5.4). Indeed, on interchanging the axis
181 and plotting $\langle \lambda \rangle T_d$ vs $\ln(\frac{L_d}{L_b})$ for synthetic data, we find that the trend in the binned data
182 follows the y=x line (Figure 2D). We also find that the best linear fit follows the y=x line
183 in the case of alanine (Figure 2B), glycerol (Figure 2- figure supplement 1A) and glucose-
184 cas (Figure 2- figure supplement 1B). A change from non-linear behavior to that of linear
185 on interchanging the axes is also observed in a related problem where growth rate (λ) and
186 inverse generation time ($\frac{1}{T_d}$) are considered (Figure 2- figure supplement 2 and Section 5.10).

187 Thus far, we showed for a range of models where birth controls division that the binned
188 data trend for $\ln(\frac{L_d}{L_b})$ as function of $\langle \lambda \rangle T_d$ is non-linear and dependent on the noise ratio $\frac{\sigma_n}{CV_\lambda}$
189 in the case of exponential growth. On interchanging the axes the binned data trend agrees
190 with the y=x line independent of the growth rate and division time noise. However, we will
191 show next that this agreement with the y=x trend cannot be used as a “smoking gun” for
192 inferring exponential growth from the data. To investigate this further, let us consider linear
193 growth, which has also been suggested to be followed by *E. coli* cells [36, 37]. The underlying
194 equation for linear growth is,

$$L_d - L_b = \lambda' T_d, \quad (3)$$

195 where λ' is the elongation speed i.e., $\frac{dL}{dt}$. For cells growing linearly, the best linear

196 fit for the plot $\langle \lambda \rangle T_d$ vs $\ln(\frac{L_d}{L_b})$ is expected to deviate from the $y=x$ line. Surprisingly, we
197 found that for the class of models where birth controls division by a strategy $f(L_b)$ and
198 cells grow linearly, the best linear fit for $\langle \lambda \rangle T_d$ vs $\ln(\frac{L_d}{L_b})$ agrees closely with the $y=x$ trend.
199 On carrying out analytical calculations based on this model, we obtain the slope and the
200 intercept of the $\langle \lambda \rangle T_d$ vs $\ln(\frac{L_d}{L_b})$ plot to be $\frac{3}{2} \ln(2) \approx 1.04$ and -0.03 respectively, which is
201 very close to that for exponential growth (see Section 5.6). This is shown for simulations
202 of linear growth with cells following an adder model in Figure 3A. Given no information
203 about the underlying model, Figure 3A could be interpreted as cells undergoing exponential
204 growth contrary to the assumption of linear growth in simulations. Thus, when handling
205 experimental data, cells undergoing either exponential or linear growth might seem to agree
206 closely with the $y=x$ trend. Deforet *et al.* [38] used the linear binned data trend in case
207 of $\langle \lambda \rangle T_d$ vs $\ln(\frac{L_d}{L_b})$ plot to infer exponential growth but as we showed in this section, the
208 linear trend does not rule out linear growth. This again reiterates our message of having a
209 generative model to guide the data analysis methods such as binning and linear regression.
210 For completeness, we also discuss the natural plot for linear growth, $\langle \lambda_{lin} \rangle T_d$ vs $l_d - l_b$ and
211 the plot obtained on interchanging the axes in Section 5.5 and Figure 3- figure supplements
212 1A, 1B. For cells growing exponentially, the best linear fit for the $\langle \lambda_{lin} \rangle T_d$ vs $l_d - l_b$ plot is
213 expected to deviate from the $y=x$ line. This is indeed what is observed in Figure 3- figure
214 supplement 1C where simulations of exponentially growing cells following the adder model
215 are presented (see Section 5.6 for extended discussion).

216 In all of the cases above, the problem at hand deals with distilling the biologically relevant
217 functional relation between two variables. However, the data is assumed to be subjected to
218 fluctuations of various sources, and it is important to ensure that the statistical construct we
219 are using (e.g. binning) is robust to these. How can we know a priori whether the statistical
220 method is appropriate and a "smoking gun" for the functional relation we are conjecturing?
221 The examples shown above suggest that performing statistical tests on synthetic data ob-

222 tained using a generative model is a convenient and powerful approach. Note that in cases
223 such as the ones studied here where analytical calculations may be performed, one may not
224 even need to perform any numerical simulations to test the validity of the methods.

225 3 Growth rate vs age plots are consistent with the un- 226 derlying growth mode.

227 In the last section, we showed that the plots $\ln(\frac{L_d}{L_b})$ vs $\langle \lambda \rangle T_d$ and $\langle \lambda \rangle T_d$ vs $\ln(\frac{L_d}{L_b})$ are not
228 decisive in identifying the mode of growth. Recent works on *B. subtilis* [39] and fission yeast
229 [40] have used differential methods of quantifying growth namely growth rate ($= \frac{1}{L} \frac{dL}{dt}$) vs
230 age plots and elongation speed ($= \frac{dL}{dt}$) vs age plots to probe the mode of growth within a
231 cell cycle. Here, L denotes the size of the cell after time t from birth in the cell cycle and
232 age denotes the ratio of time t to T_d within a cell cycle (hence it ranges from 0 to 1 by
233 construction within a cell cycle). In this section, using various models of cell growth and cell
234 cycle, we test the growth rate vs age method. For cells assumed to be growing exponentially,
235 growth rate is constant throughout the cell cycle. On averaging over multiple cell cycles, the
236 trend of binned data is expected to be a horizontal line with value equal to mean growth
237 rate which is indeed what we find in the numerical simulations of the adder and the adder
238 per origin model [17], as shown in Figure 3B. In contrast, for linearly growing cells, the
239 elongation speed is expected to remain constant. We show this constancy using numerical
240 simulations of linearly growing cells following the adder model (Figure 3- figure supplement
241 3A). In accordance with this result, the growth rate is expected to decrease with cell age
242 for linear growth. This is verified in Figure 3B by again using the numerical simulations of
243 linear growth with cells following the adder model. Thus, the two growth modes (exponential
244 and linear) could be differentiated using the growth rate vs age plot and it appears to be
245 a consistent method to obtain the mode of growth. For further details about the binning

246 method used in growth rate vs age and elongation speed vs age plots, see Section 5.7.

247 Using the validated growth rate vs age plots, we obtained the growth rate trend for
248 experimental data on *E. coli* for the three growth conditions studied in this paper (Figures
249 4A-4C). We found an increase in growth rate in all growth conditions during the course of
250 the cell cycle. One may wonder whether such an increase may be explained by the *E. coli*
251 morphology alone, due to the presence of hemispherical poles. For exponentially growing cell
252 volume and considering a geometry of *E. coli* with spherical caps at the poles, the percentage
253 increase in the growth rate of length over a cell cycle is around 3% which is significantly
254 smaller than that observed in our experimental data. Considering cell size trajectories (cell
255 size, L at time, t data) where cell lengths were tracked beyond the cell division event (by
256 considering cell size in both daughter cells), we also found that the growth rate decreases close
257 to division (age ≈ 1) and returns to a value nearly equal to that observed at the beginning
258 of cell cycle (age ≈ 0) as shown in Figure 4- figure supplements 1A-1C (see Section 5.7 for
259 extended discussion).

260 The above question of mode of growth within a cell cycle can also be analyzed in relation
261 to a specific event. Several studies have pointed to a change in growth rate at the onset of
262 constriction [41, 42]. This change in growth rate can be probed using growth rate vs time
263 plots where time is taken relative to the onset of constriction as shown in Figure 4- figure
264 supplement 2. These plots show a decrease in growth rates at the two extremes of the plot.
265 These decreases are due to inspection bias, where the growth rate trend is affected by the
266 biased contribution of cells with a higher than average generation time or equivalently slower
267 growth rate (see Section 5.8 for extended discussion). Inspection bias is also observed when
268 timing is considered relative to other cell events such as cell birth (see Section 5.8 and Figure
269 3- figure supplements 2C, 2D).

270 It might not always be possible to obtain growth rate trajectories as a function of time/cell
271 age. Godin *et al.* instead obtained the instantaneous biomass growth speed ($\frac{dM}{dt}$) as a func-

272 tion of its buoyant mass (M) [22]. On applying linear regression for instantaneous mass
273 growth speed vs mass, we expect the slope of the best linear fit obtained to provide the
274 average growth rate ($\langle \frac{1}{M} \frac{dM}{dt} \rangle$) under the assumption of exponential growth while for linear
275 growth the intercept provides the average growth speed. Using this method, biomass was
276 suggested to be growing exponentially. This method can be applied to study the length
277 growth rate within the cell cycle by plotting elongation speed as a function of length [43].
278 We find that the binned data trend of this plot follows the expected trend for linear and ex-
279 ponential growth as shown in Figure 3- figure supplement 3B and Figure 3- figure supplement
280 3D, respectively, for a cell cycle model where division is controlled via an adder mechanism
281 from birth. However, the trend obtained appears to be model-dependent as shown in Figure
282 3- figure supplement 3F where the underlying cell cycle model used in the simulations is the
283 adder per origin model. For this model, the binned data trend is found to be non-linear
284 with the growth rate speeding up at large sizes, despite the synthetic data being generated
285 for perfectly exponential growth. This non-linear trend can lead to growth rate being mis-
286 interpreted as non-exponential within the cell cycle (see Section 5.9 for details). Thus, an
287 analysis using the elongation speed vs size plot must be accompanied with an underlying
288 cell cycle model.

289 In summary, we found that the growth rate vs age plot was a consistent method to
290 determine the changes in growth rate within a cell cycle. Unlike the growth rate vs age
291 plots, the inference from the growth rate vs size plots was found to be model-dependent.
292 Using the growth rate vs age plots, we show that the length growth of *E. coli* can be faster
293 than exponential (super-exponential).

294 4 Discussion

295 Statistical methods such as binning and linear regression are useful for interpreting data and
296 generating hypotheses for biological models. However, we show in this paper that predicting
297 the relationships between experimentally measured quantities based on these methods might
298 lead to misinterpretations. Constructing a generic model and verifying the statistical analysis
299 on the synthetic data generated by this model provides a more rigorous way to mitigate these
300 risks.

301 In the paper, we provide examples in which $\ln(\frac{L_d}{L_b})$ vs $\langle \lambda \rangle T_d$ and $\langle \lambda \rangle T_d$ vs $\ln(\frac{L_d}{L_b})$ plots
302 fail as a method to infer the mode of growth. The binned data trend for $\ln(\frac{L_d}{L_b})$ vs $\langle \lambda \rangle T_d$
303 plot was found to be dependent upon the noise parameters in the class of models where
304 birth controlled division (Equation 2). We also show that $\langle \lambda \rangle T_d$ vs $\ln(\frac{L_d}{L_b})$ plot could not
305 differentiate between exponential and linear modes of growth (Figures 2D, 3A). Thus, we
306 conclude that the best linear fit for the above plots might not be a suitable method to infer
307 the mode of growth but they are just one of the many correlations which the correct cell
308 cycle model should be able to predict.

309 We found growth rate vs age and elongation speed vs age plots to be consistent methods
310 to probe growth within a cell cycle. The method was validated using simulations of various
311 cell cycle models (such as the adder, and adder per origin model, where in the latter, control
312 over division is coupled to DNA replication) and the binned growth rate trend agreed closely
313 with the underlying mode of growth for the wide range of models considered (Figure 3B). In
314 the case of growth rate vs time plots, it was important to take into consideration the effects
315 of inspection bias. We used cell cycle models to show the time regimes where inspection bias
316 could be observed (Figure 3- figure supplement 2). In the regime with negligible inspection
317 bias, we could reconcile the growth rate trend obtained using growth rate vs age (Figures 4A-
318 4C) and growth rate vs time plots (Figure 4- figure supplement 2). The authors in Ref. [31]

319 circumvent inspection bias in the elongation speed vs time from birth plots by focusing their
320 analysis on the time period from cell birth to the generation time of the fastest dividing cell.
321 The authors of Ref. [44], while investigating the division behavior in the cells undergoing
322 nutrient shift within their cell cycle, use both models and experimental data from steady-
323 state conditions to identify inspection bias. These serve as good examples of using models
324 to aid data analysis.

325 Statistics obtained from linear regression such as in Figure 1A help narrow down the
326 landscape of cell cycle models, but many have potential pitfalls lurking which might lead to
327 misinterpretations (Figure 2C, Figure 3A). There are additional issues beyond those concern-
328 ing linear regression and binning discussed here. For example, Ref. [45] discusses Simpson's
329 paradox [46] where distinct cellular sub-populations might lead to erroneous interpretation
330 of cell cycle mechanisms. Examples of such distinct sub-populations are found in asymmet-
331 rically dividing bacteria such as *M. smegmatis* [30, 47].

332 Single cell size in *E. coli* has been reported to grow exponentially [4, 14, 22–25], linearly
333 [36], bilinearly [48] or trilinearly [41]. These are inconsistent with our observations in Figures
334 4A-4C where we find that growth can be super-exponential. The non-monotonic behavior in
335 the fastest-growth condition is reminiscent of the results reported in Ref. [39] for *B. subtilis*.
336 The authors of Ref. [39] attribute the increase in growth rate to a multitude of cell cycle
337 processes such as initiation of DNA replication, divisome assembly, septum formation. In
338 the two slower growth conditions (Figures 4A-4B), we find that the growth rate increase
339 starts before the time when the septal cell wall synthesis starts i.e., the constriction event.
340 However, in the fastest growth condition (Figure 4C), the timing of growth rate increase
341 seems to coincide with the onset of constriction which is in agreement with previous findings
342 [41, 42].

343 It is important to distinguish between length growth and biomass growth. Ref. [49]
344 measures biomass and cell volume and finds the mass-density variations within the cell-cycle

345 to be small. In this paper, since we observe the length growth to be non-exponential (Figure
346 4), it remains to be seen whether biomass growth also follows a similar non-exponential
347 behavior or if it is exponential as previously suggested [22, 49].

348 In conclusion, the paper draws the attention of the readers to the careful use of statistical
349 methods such as linear regression and binning. Although shown in relation to cell growth,
350 this approach to data analysis seems ubiquitous. The general framework of carrying out data
351 analysis is presented in Figure 5. It proposes the construction of a generative model based on
352 the experimental data collected. Of course, we do not always know whether the model used
353 is an adequate description of the system. What is the fate of the methodology described here
354 in such cases? First, we should be reminded of Box's famous quote "all models are wrong,
355 some are useful". The goal of a model is not to provide as accurate a description of a system
356 as possible, but rather to capture the essence of the phenomena we are interested in and
357 stimulate further ideas and understanding. In our context, the goal of the model is to provide
358 a rigorous framework in which data analysis tools can be critically tested. If verified within
359 the model, it is by no means proof of the success of the model and the method itself, and
360 further comparisons with the data may falsify it leading to the usual (and productive) cycle
361 of model rejection and improvement via comparison with experiments. However, if the best
362 model we have at hand shows that the data analysis method is non-informative, as we have
363 shown here on several methods used to identify the mode of growth, then clearly we should
364 revise the analysis as it provides us with a non-consistent framework, where our modeling is
365 at odds with our data analysis. Furthermore, testing the methods on a simplified model is
366 still advantageous compared with the option of using the methods without any validation.
367 To mitigate the risk of using irrelevant models, in some cases it may be desirable to test the
368 analysis methods on as broad a class of models as possible as we have done in the paper, for
369 example by our use of a general value of α to describe the size-control strategy within our
370 models. Thus, guided by the model, the data analysis methods can be ultimately applied to

371 experimental data and underlying functional relationships can be inferred. Reiterating the
372 message of the authors in Ref. [8], the data analysis using this framework aims to justify
373 the methods being used, thus, reducing arbitrariness and promoting consensus among the
374 scientists working in the field.

375

5 Methods

376

5.1 Experimental methods

377 **Strain engineering:** STK13 strain ($\Delta ftsN::frt-Ypet-FtsN$, $\Delta dnaN::frt-mCherry-dnaN$) is
378 derivative of *E. coli* K12 BW27783 (CGSC#: 12119) constructed by λ -Red engineering [50]
379 and by P1 transduction [51]. For chromosomal replacement of *ftsN* with fluorescence deriva-
380 tive, we used primers carrying 40nt tails with identical sequence to the *ftsN* chromosomal
381 locus and a plasmid carrying a copy of *ypet* preceded by a kanamycin resistance cassette
382 flanked by *frt* sites (*frt-kan^R-frt-Ypet-linker*) as PCR template (a kind gift from R. Reyes-
383 Lamothe McGill University, Canada; [52]). The resulting PCR product was transformed by
384 electroporation into a strain carrying the λ -Red-expressing plasmid pKD46. Colonies were
385 selected by kanamycin resistance, verified by fluorescence microscopy and by PCR using
386 primers annealing to regions flanking *ftsN* gene. After removal of kanamycin resistance by
387 expressing the Flp recombinase from plasmid pCP20 [53], we transferred the mCherry-dnaN
388 gene fusion (BN1682 strain; a kind gift from Nynke Dekker from TUDelft, The Nether-
389 lands, [54]) into the strain by P1 transduction. To minimize the effect of the insertion on
390 the expression levels of the gene we removed the kanamycin cassette using Flp recombinase
391 expressing plasmid pCP20.

392 **Cells growth, preparation, and culturing *E. coli* in mother machine microflu-
393 idic devices:** All cells were grown and imaged in M9 minimal medium (Teknova) supple-
394 mented with 2 mM magnesium sulfate (Sigma) and corresponding carbon sources at 28°C.

395 Three different carbon sources were used: 0.5% glucose supplemented by 0.2% casamino
396 acids (Cas) (Sigma), 0.3% glycerol (Fisher) and 0.3% alanine (Fisher) supplemented with 1x
397 trace elements (Teknova).

398 For microscopy, we used mother machine microfluidic devices made of PDMS (poly-
399 dimethylsiloxane). These were fabricated following to previously described procedure [55].
400 To grow and image cells in microfluidic device, we pipetted 2-3 μ l of resuspended concen-
401 trated overnight culture of $OD_{600} \sim 0.1$ into main flow channel of the device and let cells to
402 populate the dead-end channels. Once these channels were sufficiently populated (about 1
403 hr), tubing was connected to the device, and the flow of fresh M9 medium with BSA (0.75
404 μ g/ml) was started. The flow was maintained at 5 μ l/min during the entire experiment by
405 an NE-1000 Syringe Pump (New Era Pump Systems, NY). To ensure steady-state growth,
406 the cells were left to grow in channels for at least 14 hr before imaging started.

407 **Microscopy:** A Nikon Ti-E inverted epifluorescence microscope (Nikon Instruments,
408 Japan) with a 100X (NA = 1.45) oil immersion phase contrast objective (Nikon Instru-
409 ments, Japan), was used for imaging the bacteria. Images were captured on an iXon DU897
410 EMCCD camera (Andor Technology, Ireland) and recorded using NIS-Elements software
411 (Nikon Instruments, Japan). Fluorophores were excited by a 200W Hg lamp through an
412 ND8 neutral density filter. A Chroma 41004 filtercube was used for capturing mCherry im-
413 ages, and a Chroma 41001 (Chroma Technology Corp., VT) for Ypet images. A motorized
414 stage and a perfect focus system were utilized throughout time-lapse imaging. Images in all
415 growth conditions were obtained at 4 min frame rate.

416 **Image analysis:** Image analysis was carried out using Matlab (MathWorks, MA) scripts
417 based on Matlab Image Analysis Toolbox, Optimization Toolbox, and DipImage Toolbox
418 (<https://www.diplib.org/>). Cell lengths were determined based on segmented phase contrast
419 images. Dissociation of Ypet-FtsN label from cell middle was used to determine the exact
420 timing of cell divisions.

421 Further experimental details can also be found in Ref. [32].

422 5.2 Model

423 Consider a model of cell cycle characterized by two events: cell birth and division. In our
 424 model, we assume that, barring the noise, cells tend to divide at a particular size v_d given
 425 size at birth v_b , via some regulatory mechanism. Hence, we can write v_d as a function of
 426 v_b , $f(v_b)$. Ref. [13] provides a framework to capture the regulatory mechanisms by choosing
 427 $f(v_b) = 2v_b^{1-\alpha}v_0^\alpha$. v_0 is the typical size at birth and α captures the strength of regulation
 428 strategy. $\alpha = 0$ corresponds to the timer model where division occurs after a constant time
 429 from birth, and $\alpha = 1$ is the sizer where a cell divides on reaching a critical size. $\alpha = 1/2$ can
 430 be shown to be equivalent to an adder where division is controlled by addition of constant
 431 size from birth [13]. From here on, we would be using the length of the cell (L_b , L_d , etc.) as
 432 a proxy for size (v_b , v_d , etc.). All of the variable definitions are summarized in Table S1. We
 433 also define $l_b = \frac{L_b}{\langle L_b \rangle}$ and $l_d = \frac{L_d}{\langle L_b \rangle}$. Using this, we can write the division strategy $f(l_b)$ to be l_d
 434 $= f(l_b) = 2 l_b^{1-\alpha}$. The total division size obtained will be a combination of $f(l_b)$ and noise in
 435 the division timing, the source of which could be the stochasticity in biochemical reactions
 436 controlling division.

437 We will assume that division is perfectly symmetric i.e., size at birth in the $(n + 1)^{th}$
 438 generation (l_b^{n+1}) is half of size at division in the n^{th} generation (l_d^n). Using the size additive
 439 division timing noise ($\zeta_s(0, \sigma_{bd})$) and $f(l_b)$ specified above, we obtain,

$$x_{n+1} = (1 - \alpha)x_n + \ln \left(1 + \frac{\zeta_s(0, \sigma_{bd})}{2(1 + x_n)^{1-\alpha}} \right), \quad (4)$$

440 where $x_n = \ln(l_b^n)$. Size at birth (L_b) is narrowly distributed, hence $l_b \approx 1$ and we can write

441 $x = \ln(l_b) = \ln(1 + \delta)$ where δ is a small number. We obtain $x \ll 1$ and,

$$x \approx \delta = l_b - 1. \quad (5)$$

442 The size additive noise, $\zeta_s(0, \sigma_{bd})$ is assumed to be small and has a normal distribution with
443 mean 0 and standard deviation σ_{bd} . Note that σ_{bd} is a dimensionless quantity. Since $\zeta_s(0, \sigma_{bd})$
444 is assumed to be small and $x_n \ll 1$, we can Taylor expand the last term of Equation 4 to
445 first order,

$$x_{n+1} \approx (1 - \alpha)x_n + \frac{\zeta_s(0, \sigma_{bd})}{2}. \quad (6)$$

446 Equation 6 shows a recursive relation for cell size and it is agnostic of the mode of growth.
447 We will show later for exponential growth that replacing the size additive noise with time
448 additive noise does not change the structure of Equation 6.

449 5.3 Exponential growth

450 Next, we will try to obtain the generation time (T_d) in the case of exponentially growing
451 cells. For exponential growth, the time at division T_d is given by,

$$T_d = \frac{1}{\lambda} \ln\left(\frac{L_d}{L_b}\right). \quad (7)$$

452 For simplicity, we will assume a constant growth rate (λ) within the cell-cycle. Growth rate
453 is fixed at the start of the cell-cycle and is given by $\lambda = \langle \lambda \rangle + \langle \lambda \rangle \xi(0, CV_\lambda)$, where $\langle \lambda \rangle$ is
454 the mean growth rate and $\xi(0, CV_\lambda)$ is assumed to be small with a normal distribution that
455 has mean 0 and standard deviation CV_λ . CV_λ denotes the coefficient of variation (CV) of
456 the growth rate. This captures the variability in growth rate within cells arising from the
457 stochastic nature of biochemical reactions occurring within the cell.

458 **5.3.1 Size additive noise**

459 Here we will calculate the generation time using the division strategy $f(l_b)$ and a size additive
 460 division timing noise ($\zeta_s(0, \sigma_{bd})$) as described previously. On substituting $L_d = (f(l_b) +$
 461 $\zeta_s)\langle L_b \rangle$ into Equation 7 we obtain,

$$T_d = \frac{1}{\langle \lambda \rangle + \langle \lambda \rangle \xi(0, CV_\lambda)} \ln\left(\frac{2l_b^{1-\alpha} + \zeta_s(0, \sigma_{bd})}{l_b}\right), \quad (8)$$

462 where the size additive noise ($\zeta_s(0, \sigma_{bd})$) is Gaussian with mean 0 and standard deviation
 463 σ_{bd} .

464 The noise $\zeta_s(0, \sigma_{bd})$ is assumed to be small, and we obtain to first order,

$$T_d \approx \frac{1}{\lambda} \left(\ln(2) - \alpha x_n + \frac{\zeta_s(0, \sigma_{bd})}{2(1+x_n)^{1-\alpha}} \right). \quad (9)$$

465 Since $x_n \ll 0$, on Taylor expanding $\frac{1}{(1+x_n)^{1-\alpha}}$ to first order,

$$T_d \approx \frac{1}{\lambda} \left(\ln(2) - \alpha x_n + \frac{\zeta_s(0, \sigma_{bd})}{2} (1 + (1 - \alpha)x_n) \right). \quad (10)$$

466 Assuming noise in growth rate to be small and expanding to first order, we obtain,

$$T_d \approx \frac{1}{\langle \lambda \rangle} \left(\ln(2) - \alpha x_n - \ln(2) \xi(0, CV_\lambda) + \frac{\zeta_s(0, \sigma_{bd})}{2} \right). \quad (11)$$

467 Equation 11 gives the generation time for the class of models where birth controls division
 468 under the assumption that growth is exponential.

469 **5.3.2 Time additive noise**

470 Next, we ensure that the recursive relation for size at birth and the expression for the
 471 generation time given by Equations 6 and 11, respectively, are robust to the nature of noise

472 assumed. In this section, the generation time is obtained using the division strategy $f(l_b)$ as
 473 described previously along with a time additive division timing noise $(\frac{\zeta}{\langle \lambda \rangle})$. In such a case,
 474 T_d is obtained to be,

$$T_d = \frac{1}{\lambda}(\ln(2) - \alpha x_n) + \frac{\zeta(0, \sigma_n)}{\langle \lambda \rangle}. \quad (12)$$

475 The time additive noise, $\frac{\zeta(0, \sigma_n)}{\langle \lambda \rangle}$, is assumed to be small and has a normal distribution with
 476 mean 0 and standard deviation $\frac{\sigma_n}{\langle \lambda \rangle}$. Note that σ_n is a dimensionless quantity.

477 Assuming noise in growth rate to be small, we find T_d to first order to be,

$$T_d \approx \frac{1}{\langle \lambda \rangle} (\ln(2) - \alpha x_n - \ln(2)\xi(0, CV_\lambda) + \zeta(0, \sigma_n)). \quad (13)$$

478 Equation 13 is same as Equation 11, if the time additive noise term, $\zeta(0, \sigma_n)$, in Equation
 479 12 is replaced by $\zeta_s(0, \sigma_{bd})/2$. Using Equation 13, the variance in T_d (σ_t^2) is,

$$\sigma_t^2 = \frac{1}{\langle \lambda \rangle^2} \left(\ln^2(2)CV_\lambda^2 + \frac{2\sigma_n^2}{2 - \alpha} \right). \quad (14)$$

480 For exponential growth, we also find,

$$\ln\left(\frac{L_d}{L_b}\right) = x_{n+1} - x_n + \ln(2) = \lambda T_d. \quad (15)$$

481 On substituting Equation 12 into Equation 15 we obtain to first order,

$$x_{n+1} \approx (1 - \alpha)x_n + \zeta(0, \sigma_n). \quad (16)$$

482 On replacing the time additive noise term, $\zeta(0, \sigma_n)$, in Equation 16 with $\zeta_s(0, \sigma_{bd})/2$, we
 483 recover the recursive relation for size at birth obtained in the case of size additive noise
 484 shown in Equation 6. Hence, the model is insensitive to noise being size additive or time
 485 additive with a simple mapping for going from one noise type to another in the small noise

486 limit.

487 At steady state, x has a normal distribution with mean 0 and variance σ_x^2 whose value is
 488 given by,

$$\sigma_x^2 = \frac{\sigma_n^2}{\alpha(2 - \alpha)}. \quad (17)$$

489 We note that some of the derivations above have also been presented in Ref. [16], but are
 490 provided here for completeness.

491 **5.4 Predicting the results of statistical constructs applied on $\ln(\frac{L_d}{L_b})$**

492 **vs $\langle \lambda \rangle T_d$ and $\langle \lambda \rangle T_d$ vs $\ln(\frac{L_d}{L_b})$**

493 **5.4.1 Obtaining the best linear fit**

494 Next, we calculate the equation for the best linear fit for the choice of $\ln(\frac{L_d}{L_b})$ as y-axis and
 495 $\langle \lambda \rangle T_d$ as x-axis and vice versa. For simplicity, in this section, we will consider time additive
 496 division timing noise. However, the results obtained here will hold for size additive noise as
 497 well because the model is robust to the type of noise added as shown in the previous section.

498 First, we calculate the correlation coefficient (ρ_{exp}) for $\ln(\frac{L_d}{L_b})$ and time of division T_d ,

$$\rho_{exp} = \frac{\langle (\ln(\frac{L_d}{L_b}) - \langle \ln(\frac{L_d}{L_b}) \rangle)(T_d - \langle T_d \rangle) \rangle}{\sigma_l \sigma_t}, \quad (18)$$

499 where σ_l is the standard deviation in $\ln(\frac{L_d}{L_b})$. Using Equations 15 and 16 we obtain,

$$\ln(\frac{L_d}{L_b}) \approx \ln(2) - \alpha x_n + \zeta(0, \sigma_n). \quad (19)$$

Substituting Equations 13 and 19 into the numerator of Equation 18,

$$\begin{aligned} & \langle (\ln(\frac{L_d}{L_b}) - \langle \ln(\frac{L_d}{L_b}) \rangle)(T_d - \langle T_d \rangle) \rangle \\ &= \langle (-\alpha x_n + \zeta(0, \sigma_n)) \frac{(-\alpha x_n - \ln(2)\xi(0, CV_\lambda) + \zeta(0, \sigma_n))}{\langle \lambda \rangle} \rangle. \quad (20) \end{aligned}$$

500 As the terms $\zeta(0, \sigma_n)$, $\xi(0, CV_\lambda)$ and x_n are independent of each other, $\langle \xi(0, CV_\lambda) \zeta(0, \sigma_n) \rangle =$
501 0 , $\langle \xi(0, CV_\lambda) x_n \rangle = 0$ and $\langle x_n \zeta(0, \sigma_n) \rangle = 0$. Equation 20 simplifies to,

$$\langle (\ln(\frac{L_d}{L_b}) - \langle \ln(\frac{L_d}{L_b}) \rangle)(T_d - \langle T_d \rangle) \rangle = (\alpha^2 \sigma_x^2 + \sigma_n^2) \frac{1}{\langle \lambda \rangle}. \quad (21)$$

502 The variance of $\ln(\frac{L_d}{L_b})$ obtained using Equation 19 is,

$$\sigma_l^2 = \alpha^2 \sigma_x^2 + \sigma_n^2 = \frac{2\sigma_n^2}{2 - \alpha}. \quad (22)$$

503 Inserting Equations 14, 21 and 22 into Equation 18, we get,

$$\rho_{exp} = \sqrt{\frac{1}{1 + \frac{(1 - \frac{\alpha}{2}) \ln^2(2) CV_\lambda^2}{\sigma_n^2}}}. \quad (23)$$

504 The slope of a linear regression line is given by,

$$m = \rho \frac{\sigma_y}{\sigma_x}, \quad (24)$$

505 where σ_x , σ_y and ρ are the standard deviation of the x-variable, the standard deviation of
506 the y-variable and the correlation coefficient of the (x,y) pair, respectively. The intercept is,

$$c = \langle y \rangle - m \langle x \rangle. \quad (25)$$

507 On the x-axis, we plot $\langle \lambda \rangle T_d$ and the y-axis is chosen as $\ln(\frac{L_d}{L_b})$. The slope for this choice
 508 (m_{tl}) can be calculated by,

$$m_{tl} = \rho_{exp} \frac{\sigma_l}{\sigma_t \langle \lambda \rangle}. \quad (26)$$

509 On substituting the values we get,

$$m_{tl} = \frac{1}{1 + \frac{(1 - \frac{\alpha}{2}) \ln^2(2) CV_\lambda^2}{\sigma_n^2}}. \quad (27)$$

510 Only for $CV_\lambda \ll \sigma_n$ we would expect a slope close to 1.

511 The intercept (c_{tl}) for the $\ln(\frac{L_d}{L_b})$ vs $\langle \lambda \rangle T_d$ plot is given by,

$$c_{tl} = \langle \ln(\frac{L_d}{L_b}) \rangle - m_{tl} \langle \langle \lambda \rangle T_d \rangle = \ln(2) \left(1 - \frac{1}{1 + \frac{(1 - \frac{\alpha}{2}) \ln^2(2) CV_\lambda^2}{\sigma_n^2}} \right). \quad (28)$$

512 However, if we choose the x-axis as $\ln(\frac{L_d}{L_b})$ and the y-axis is chosen as $\langle \lambda \rangle T_d$, we obtain the
 513 slope m_{lt} ,

$$m_{lt} = \rho_{exp} \frac{\sigma_t \langle \lambda \rangle}{\sigma_l}. \quad (29)$$

514 On substituting the values we obtain $m_{lt} = 1$ independent of the noise parameters and find
 515 that the intercept is zero.

516 5.4.2 Non-linearity in binned data

517 In the Main text, for the plot $\ln(\frac{L_d}{L_b})$ vs $\langle \lambda \rangle T_d$, we find the binned data to be non-linear (see
 518 Figure 2C of the Main text). In this section, we explain the non-linearity observed using the
 519 model developed in the previous sections.

520 Binning data based on the x-axis means taking an average of the y-variable conditioned
 521 on the value of the x-variable. Mathematically, this amounts to calculating $\mathbb{E}[y | x]$ i.e.,
 522 the conditional expectation of the y-variable given that x is fixed. In our case, we need to

523 calculate $\mathbb{E}[\ln(\frac{L_d}{L_b}) \mid \langle \lambda \rangle T_d]$. $\ln(\frac{L_d}{L_b}) = \lambda T_d$ by definition of exponential growth, hence,

$$\mathbb{E}[\ln(\frac{L_d}{L_b}) \mid \langle \lambda \rangle T_d] = \mathbb{E}[\lambda T_d \mid \langle \lambda \rangle T_d]. \quad (30)$$

524 Since T_d is fixed, this is equivalent to calculating $\mathbb{E}[\lambda \mid T_d]$. Using Equation 13,

$$\mathbb{E}[\lambda \mid T_d] = \frac{\int_{-\infty}^{\infty} \int_{-\infty}^{\infty} \int_{-\infty}^{\infty} \lambda p(x, \xi, \zeta) \delta(T_d - (\frac{\ln(2)}{\langle \lambda \rangle} - \alpha \frac{x}{\langle \lambda \rangle} - \frac{\ln(2)\xi}{\langle \lambda \rangle} + \frac{\zeta}{\langle \lambda \rangle})) dx d\xi d\zeta}{\int_{-\infty}^{\infty} \int_{-\infty}^{\infty} \int_{-\infty}^{\infty} p(x, \xi, \zeta) \delta(T_d - (\frac{\ln(2)}{\langle \lambda \rangle} - \alpha \frac{x}{\langle \lambda \rangle} - \frac{\ln(2)\xi}{\langle \lambda \rangle} + \frac{\zeta}{\langle \lambda \rangle})) dx d\xi d\zeta}. \quad (31)$$

$p(x, \xi, \zeta)$ is the joint probability distribution of x and noise parameters ξ and ζ . Since, they are independent of each other, the joint distribution is product of the individual distributions $f_1(x)$, $f_2(\xi)$ and $f_3(\zeta)$, the distributions being Gaussian with mean 0 and standard deviation σ_x , CV_λ and σ_n , respectively. σ_x , σ_n are related by Equation 17. Since x , ξ , and ζ are narrowly distributed around zero, the contribution from large positive or negative values is extremely small. This ensures that T_d is also close to its mean and non-negative despite the limits of the integral being $-\infty$ to ∞ . Using $\lambda = \langle \lambda \rangle + \langle \lambda \rangle \xi(0, CV_\lambda)$ in Equation 31,

$$\begin{aligned} & \mathbb{E}[\lambda \mid T_d] \\ &= \langle \lambda \rangle \left(1 + \frac{\int_{-\infty}^{\infty} \int_{-\infty}^{\infty} \int_{-\infty}^{\infty} \xi f_1(x) f_2(\xi) f_3(\zeta) \delta(T_d - (\frac{\ln(2)}{\langle \lambda \rangle} - \alpha \frac{x}{\langle \lambda \rangle} - \frac{\ln(2)\xi}{\langle \lambda \rangle} + \frac{\zeta}{\langle \lambda \rangle})) dx d\xi d\zeta}{\int_{-\infty}^{\infty} \int_{-\infty}^{\infty} \int_{-\infty}^{\infty} f_1(x) f_2(\xi) f_3(\zeta) \delta(T_d - (\frac{\ln(2)}{\langle \lambda \rangle} - \alpha \frac{x}{\langle \lambda \rangle} - \frac{\ln(2)\xi}{\langle \lambda \rangle} + \frac{\zeta}{\langle \lambda \rangle})) dx d\xi d\zeta} \right). \end{aligned} \quad (32)$$

525 On evaluating the integrals, we obtain,

$$\mathbb{E}[\lambda \mid T_d] = \langle \lambda \rangle \left(1 + \frac{1}{1 + \frac{2}{2-\alpha} \frac{\sigma_n^2}{CV_\lambda^2 \ln^2(2)}} - \frac{\frac{\langle \lambda \rangle T_d}{\ln(2)}}{1 + \frac{2}{2-\alpha} \frac{\sigma_n^2}{CV_\lambda^2 \ln^2(2)}} \right). \quad (33)$$

526 Thus, the trend of binned data is found to be,

$$\mathbb{E}[\ln(\frac{L_d}{L_b}) \mid \langle \lambda \rangle T_d] = \langle \lambda \rangle T_d \left(1 + \frac{1}{1 + \frac{2}{2-\alpha} \frac{\sigma_n^2}{CV_\lambda^2 \ln^2(2)}} - \frac{\frac{\langle \lambda \rangle T_d}{\ln(2)}}{1 + \frac{2}{2-\alpha} \frac{\sigma_n^2}{CV_\lambda^2 \ln^2(2)}} \right). \quad (34)$$

527 In the regime $CV_\lambda \ll \sigma_n$, the last two terms on the RHS of Equation 34 vanish and the
 528 binned data follows the trend $y=x$.

529 For the $\langle \lambda \rangle T_d$ vs $\ln(\frac{L_d}{L_b})$ plot, we need to calculate $\mathbb{E}[\langle \lambda \rangle T_d \mid \ln(\frac{L_d}{L_b})]$. Using Equations 13
 530 and 19, we obtain,

$$\langle \lambda \rangle T_d = \ln(\frac{L_d}{L_b}) - \ln(2)\xi(0, CV_\lambda). \quad (35)$$

$\ln(\frac{L_d}{L_b})$ is independent of $\xi(0, CV_\lambda)$. Using this, we can write $\mathbb{E}[\langle \lambda \rangle T_d \mid \ln(\frac{L_d}{L_b})]$ as,

$$\begin{aligned} \mathbb{E}[\langle \lambda \rangle T_d \mid \ln(\frac{L_d}{L_b})] \\ = \frac{\int_{-\infty}^{\infty} \int_{-\infty}^{\infty} (\langle \lambda \rangle T_d) f_2(\xi) f_4(\ln(\frac{L_d}{L_b})) \delta\left(\langle \lambda \rangle T_d - (\ln(\frac{L_d}{L_b}) - \ln(2)\xi)\right) d(\langle \lambda \rangle T_d) d\xi}{f_4(\ln(\frac{L_d}{L_b}))}. \end{aligned} \quad (36)$$

531 Note that the integral over $\langle \lambda \rangle T_d$ goes from $-\infty$ to ∞ although $\langle \lambda \rangle T_d$ cannot be negative.
 532 As before, this is not an issue because we assume $\langle \lambda \rangle T_d$ to be tightly regulated around $\ln(2)$
 533 and the contribution to the integral from $-\infty$ to 0 is negligible. $f_4(\ln(\frac{L_d}{L_b}))$ denotes the
 534 probability distribution for $\ln(\frac{L_d}{L_b})$, the distribution being Gaussian with mean $\ln(2)$, and
 535 standard deviation σ_l which is calculated in Equation 22. Putting the Gaussian form of
 536 $f_2(\xi)$ into the integral and simplifying we get,

$$\mathbb{E}[\langle \lambda \rangle T_d \mid \ln(\frac{L_d}{L_b})] = \ln(\frac{L_d}{L_b}). \quad (37)$$

537 The trend of binned data to first order in noise and x is $\mathbb{E}[\langle \lambda \rangle T_d \mid \ln(\frac{L_d}{L_b})] = \ln(\frac{L_d}{L_b})$. This is
 538 shown in Figure 2D of the Main text where the binned data follows the $y=x$ line.

539 5.5 Linear growth

540 In this section, we will focus on finding the equation of the best linear fit for relevant plots
 541 in the case of linear growth. The time at division for linear growth is given by,

$$T_d = \frac{L_d - L_b}{\lambda'}. \quad (38)$$

542 Note that λ' has units of [length/time] and is defined as the elongation speed. This is
 543 different from the exponential growth rate which has units [1/time]. Here, we will work with
 544 the normalized length at birth (l_b) and division (l_d),

$$T_d = \frac{l_d - l_b}{\lambda_{lin}}. \quad (39)$$

545 Consider the normalized elongation speed to be $\lambda_{lin} = \langle \lambda_{lin} \rangle + \langle \lambda_{lin} \rangle \xi_{lin}(0, CV_{\lambda,lin})$, where
 546 $\langle \lambda_{lin} \rangle$ is the mean normalized elongation speed for a lineage of cells and $\xi_{lin}(0, CV_{\lambda,lin})$ is
 547 normally distributed with mean 0 and standard deviation $CV_{\lambda,lin}$. Thus, the CV of elongation
 548 speed is $CV_{\lambda,lin}$. The regulation strategy which the cell undertakes is equivalent to that in
 549 previous sections and is given by $g(l_b) = 2 + 2(1 - \alpha)(l_b - 1)$. Note that we can obtain $g(l_b)$
 550 by Taylor expanding $f(l_b)$ around $l_b = 1$. Using the regulation strategy $g(l_b)$ and adding a
 551 size additive noise $\zeta_s(0, \sigma_{bd})$ which is independent of l_b , we find,

$$T_d = \frac{2 + 2(1 - \alpha)(l_b^n - 1) + \zeta_s(0, \sigma_{bd}) - l_b^n}{\langle \lambda_{lin} \rangle (1 + \xi_{lin}(0, CV_{\lambda,lin}))}. \quad (40)$$

552 Note that we chose size additive division timing noise ($\zeta_s(0, \sigma_{bd})$) for convenience in this
 553 section. However, it can be shown as done previously that the model is robust to the noise
 554 in division timing being size additive or time additive. Assuming that the noise terms

555 $\xi_{lin}(0, CV_{\lambda,lin})$ and $\zeta_s(0, \sigma_{bd})$ are small, we obtain to first order,

$$T_d \approx \frac{(1 - 2\alpha)(l_b - 1) + 1 + \zeta_s(0, \sigma_{bd}) - \xi_{lin}(0, CV_{\lambda,lin})}{\langle \lambda_{lin} \rangle}. \quad (41)$$

556 The terms l_b , $\zeta_s(0, \sigma_{bd})$ and $\xi_{lin}(0, CV_{\lambda,lin})$ are independent of each other. The standard
557 deviation of T_d (σ_t) can be calculated to be,

$$\sigma_t^2 = \frac{(1 - 2\alpha)^2 \sigma_b^2 + \sigma_{bd}^2 + CV_{\lambda,lin}^2}{\langle \lambda_{lin} \rangle^2}. \quad (42)$$

558 Assuming perfectly symmetric division and using $l_d^n = g(l_b^n) + \zeta_s(0, \sigma_{bd})$, we find the recursive
559 relation for l_b^n to be,

$$l_d^n - l_b^n = 2l_b^{n+1} - l_b^n = (1 - 2\alpha)l_b^n + 2\alpha + \zeta_s(0, \sigma_{bd}). \quad (43)$$

560 Note that Equation 43 is the same as Equation 6 under the approximation $x_n = l_b^n - 1$. At
561 steady state, the standard deviation of l_b is denoted by σ_b and using Equation 43 its value
562 is obtained to be,

$$\sigma_b^2 = \frac{\sigma_{bd}^2}{4\alpha(2 - \alpha)}. \quad (44)$$

563 Similarly, the standard deviation of $l_d - l_b$, or equivalently $\lambda_{lin}T_d$, denoted by $\sigma_{l,lin}$, is calculated
564 to be,

$$\sigma_{l,lin}^2 = \frac{4\alpha + 1}{4\alpha(2 - \alpha)} \sigma_{bd}^2. \quad (45)$$

565 For linear growth, a natural plot is $l_d - l_b$ vs $\langle \lambda_{lin} \rangle T_d$ (reminiscent of the $\ln(\frac{L_d}{L_b})$ vs $\langle \lambda \rangle T_d$ plot
566 for exponential growth). To calculate the slope of the best linear fit, we have to calculate
567 the correlation coefficient ρ_{lin} given by,

$$\rho_{lin} = \frac{\langle (l_d - l_b - \langle l_d - l_b \rangle) (\langle \lambda_{lin} \rangle T_d - \langle \langle \lambda_{lin} \rangle T_d \rangle) \rangle}{\langle \lambda_{lin} \rangle \sigma_{l,lin} \sigma_t}. \quad (46)$$

568 Again using the independence of terms l_b , $\zeta_s(0, \sigma_{bd})$ and $\xi_{lin}(0, CV_{\lambda,lin})$ from each other, we

569 get,

$$\rho_{lin} = \frac{(1 - 2\alpha)^2 \sigma_b^2 + \sigma_{bd}^2}{\langle \lambda_{lin} \rangle \sigma_{l,lin} \sigma_t} = \frac{\sigma_{l,lin}}{\langle \lambda_{lin} \rangle \sigma_t}. \quad (47)$$

570 The slope of best linear fit for the plot $l_d - l_b$ vs $\langle \lambda_{lin} \rangle T_d$ is given by,

$$m_{tl,lin} = \rho_{lin} \frac{\sigma_{l,lin}}{\langle \lambda_{lin} \rangle \sigma_t} = \frac{1}{1 + \frac{CV_{\lambda,lin}^2 4\alpha(2-\alpha)}{\sigma_{bd}^2 (4\alpha+1)}}. \quad (48)$$

571 The intercept $c_{tl,lin}$ is found to be,

$$c_{tl,lin} = \langle l_d - l_b \rangle - m_{tl,lin} \langle \langle \lambda_{lin} \rangle T_d \rangle = 1 - \frac{1}{1 + \frac{CV_{\lambda,lin}^2 4\alpha(2-\alpha)}{\sigma_{bd}^2 (4\alpha+1)}}. \quad (49)$$

572 On flipping the axis, the slope ($m_{lt,lin}$) for the plot $\langle \lambda_{lin} \rangle T_d$ vs $l_d - l_b$ is obtained to be,

$$m_{lt,lin} = \rho_{lin} \frac{\langle \lambda_{lin} \rangle \sigma_t}{\sigma_{l,lin}} = 1. \quad (50)$$

573 The intercept $c_{lt,lin}$ is found to be,

$$c_{lt,lin} = \langle \langle \lambda_{lin} \rangle T_d \rangle - m_{lt,lin} \langle l_d - l_b \rangle = 0. \quad (51)$$

574 The best linear fit for the $\langle \lambda_{lin} \rangle T_d$ vs $l_d - l_b$ plot follows the trend y=x.

575 Simulations of the adder model for linearly growing cells were carried out. The deviation
 576 of the best linear fit for the $l_d - l_b$ vs $\langle \lambda_{lin} \rangle T_d$ plot from the y=x line is shown in Figure 3-
 577 figure supplement 1A, while in Figure 3- figure supplement 1B, the best linear fit for the plot
 578 $\langle \lambda_{lin} \rangle T_d$ vs $l_d - l_b$ is shown to agree with the y=x line.

579 5.6 Differentiating linear from exponential growth

580 In this section, we explore the equation for the best linear fit of $\langle \lambda_{lin} \rangle T_d$ vs $l_d - l_b$ plot in
 581 the case of exponential growth and $\langle \lambda \rangle T_d$ vs $\ln(\frac{L_d}{L_b})$ plot for linear growth. Intuitively, we
 582 expect the best linear fit in both cases to deviate from the y=x line. In this section, we will
 583 calculate the best linear fit explicitly. Surprisingly, we will find that, in the case of linear
 584 growth, the best linear fit for the $\langle \lambda \rangle T_d$ vs $\ln(\frac{L_d}{L_b})$ plot follows the y=x line closely.

585 Let us begin with exponential growth with growth rate, $\lambda = \langle \lambda \rangle + \langle \lambda \rangle \xi(0, CV_\lambda)$ as
 586 defined previously. Again, $\xi(0, CV_\lambda)$ has a normal distribution with mean 0 and standard
 587 deviation CV_λ , it being the CV of the growth rate. The time at division is given by Equation
 588 7. The average growth rate $\langle \lambda \rangle = \langle \frac{\ln(2)}{T_d} \rangle \approx \frac{\ln(2)}{\langle T_d \rangle}$. For exponential growth, we will plot
 589 $\langle \lambda_{lin} \rangle T_d$ vs $l_d - l_b$. As previously defined, $\langle \lambda_{lin} \rangle$ is the mean normalized elongation speed and
 590 $\langle \lambda_{lin} \rangle = \langle \frac{1}{T_d} \rangle \approx \frac{1}{\langle T_d \rangle}$. $\langle \lambda_{lin} \rangle$ is related to $\langle \lambda \rangle$ by,

$$\langle \lambda_{lin} \rangle = \frac{\langle \lambda \rangle}{\ln(2)}. \quad (52)$$

591 $l_d - l_b$ can be calculated by using the regulation strategy $f(l_b)$ introduced in Section 5.2 and
 592 a normally distributed size additive noise $\zeta_s(0, \sigma_{bd})$. Note that we have chosen the noise in
 593 division timing to be size additive. However, the model is robust to the choice of type of
 594 noise as we showed in Section 5.3. Using Equations 5 and 6 we obtain,

$$l_d^n - l_b^n \approx 1 + (1 - 2\alpha)x_n + \zeta_s(0, \sigma_{bd}). \quad (53)$$

595 Using Equation 11, $\langle \lambda_{lin} \rangle T_d$ is obtained to be,

$$\langle \lambda_{lin} \rangle T_d = 1 - \frac{\alpha x}{\ln(2)} - \xi(0, CV_\lambda) + \frac{\zeta_s(0, \sigma_{bd})}{2 \ln(2)}. \quad (54)$$

596 To calculate the expression for $m_{lt,lin}$, the slope of the best linear fit for $\langle \lambda_{lin} \rangle T_d$ vs $l_d - l_b$ plot,

597 we first calculate ρ_{lin} given by Equation 46. The expression for $\sigma_{l,lin}$ (standard deviation of
 598 $l_d - l_b$) and σ_t (standard deviation of T_d) are found to be,

$$\sigma_{l,lin}^2 = (1 - 2\alpha)^2 \sigma_x^2 + \sigma_{bd}^2, \quad (55)$$

599

$$\sigma_t^2 = \frac{1}{\langle \lambda_{lin} \rangle^2} \left(\left(\frac{\alpha \sigma_x}{\ln(2)} \right)^2 + CV_\lambda^2 + \left(\frac{\sigma_{bd}}{2 \ln(2)} \right)^2 \right). \quad (56)$$

600 σ_x is related to σ_n via Equation 17. In Section 5.3, we also showed that $\sigma_n = \frac{\sigma_{bd}}{2}$. Using
 601 these, we can write,

$$\sigma_x^2 = \frac{\sigma_{bd}^2}{4\alpha(2 - \alpha)}. \quad (57)$$

602 Now using the expressions for σ_t , $\sigma_{l,lin}$ and the fact that x , $\xi(0, CV_\lambda)$ and $\zeta_s(0, \sigma_{bd})$ are
 603 independent of each other, we get,

$$\rho_{lin} = \frac{\frac{(2\alpha-1)\alpha\sigma_x^2}{\ln(2)} + \frac{\sigma_{bd}^2}{2\ln(2)}}{\langle \lambda_{lin} \rangle \sigma_{l,lin} \sigma_t}. \quad (58)$$

604 For the plot $\langle \lambda_{lin} \rangle T_d$ vs $l_d - l_b$, the slope $m_{lt,lin}$ is given by,

$$m_{lt,lin} = \rho_{lin} \frac{\sigma_t \langle \lambda_{lin} \rangle}{\sigma_{l,lin}} = \frac{\frac{(2\alpha-1)\alpha\sigma_x^2}{\ln(2)} + \frac{\sigma_{bd}^2}{2\ln(2)}}{\sigma_{l,lin}^2}. \quad (59)$$

605 Inserting Equation 55 into Equation 59 and substituting σ_x^2 given by Equation 57, we obtain,

$$m_{lt,lin} = \frac{1}{\ln(2)} \frac{3\alpha}{4\alpha + 1}. \quad (60)$$

606 The intercept $c_{lt,lin}$ is found to be,

$$c_{lt,lin} = \langle \langle \lambda_{lin} \rangle T_d \rangle - m_{lt,lin} \langle l_d - l_b \rangle = 1 - \frac{1}{\ln(2)} \frac{3\alpha}{4\alpha + 1}. \quad (61)$$

607 For the adder model ($\alpha = \frac{1}{2}$), we get the value of slope $m_{lin,lt} = \frac{1}{2\ln(2)} \approx 0.7213$ and intercept
608 $c_{lin,lt} = 1 - \frac{1}{2\ln(2)} \approx 0.279$. This is different from the best linear fit obtained for same
609 regulatory mechanism controlling division in linearly growing cells where we found that the
610 best linear fit follows the $y=x$ line. Intuitively, we expect the best linear fit of $\langle \lambda_{lin} \rangle T_d$ vs
611 $l_d - l_b$ plot to deviate from $y=x$ line in the case of exponential growth. We showed analytically
612 that for a class of models where birth controls division, it is indeed the case. This is also
613 shown using simulations of the adder model in Figure 3- figure supplement 1C.

614 In Section 5.4.1, we found the best linear fit for $\langle \lambda \rangle T_d$ vs $\ln(\frac{L_d}{L_b})$ plot to follow the $y=x$
615 line for exponentially growing cells where division is regulated by birth event via regulation
616 strategy $f(l_b)$. Next, we calculate the equation for the best linear fit of $\langle \lambda \rangle T_d$ vs $\ln(\frac{L_d}{L_b})$
617 plot given growth is linear. The model for division control will be same as that in Section
618 5.5 i.e., the regulation strategy for division is given by $g(l_b) = 2 + 2(1 - \alpha)(l_b - 1)$ which
619 is also equivalent to $f(l_b)$. The linearly growing cells grow with elongation speed $\lambda_{lin} =$
620 $\langle \lambda_{lin} \rangle (1 + \xi_{lin}(0, CV_{\lambda,lin}))$. As discussed before, $\xi_{lin}(0, CV_{\lambda,lin})$ has a normal distribution with
621 mean 0 and standard deviation $CV_{\lambda,lin}$, it being the CV of the elongation speed. Using
622 Equations 5 and 6, we get,

$$\ln\left(\frac{L_d}{L_b}\right) = \ln(2) - \alpha x^n + \frac{\zeta_s(0, \sigma_{bd})}{2}. \quad (62)$$

623 Using Equations 5 and 52, we obtain from Equation 41,

$$\langle \lambda \rangle T_d = \ln(2) + (1 - 2\alpha) \ln(2)x + \ln(2)\zeta_s(0, \sigma_{bd}) - \ln(2)\xi_{lin}(0, CV_{\lambda,lin}). \quad (63)$$

624 Since x , $\xi_{lin}(0, CV_{\lambda,lin})$ and $\zeta_s(0, \sigma_{bd})$ are uncorrelated, the standard deviation of $\ln(\frac{L_d}{L_b})$ and
625 T_d denoted by σ_l and σ_t respectively are calculated to be,

$$\sigma_l^2 = \alpha^2 \sigma_x^2 + \frac{\sigma_{bd}^2}{4}, \quad (64)$$

$$\sigma_t^2 = \frac{\ln^2(2)}{\langle \lambda \rangle^2} ((1 - 2\alpha)^2 \sigma_x^2 + \sigma_{bd}^2 + CV_{\lambda,lin}^2). \quad (65)$$

626 We calculate the correlation coefficient for the pair $(\ln(\frac{L_d}{L_b}), \langle \lambda \rangle T_d)$. Since the correlation
627 coefficient is unaffected by multiplying one of the variables with a positive constant, we can
628 calculate the correlation coefficient for the pair $(\ln(\frac{L_d}{L_b}), T_d)$ or ρ_{exp} as given by Equation 18.
629 Using the independence of terms x , $\xi_{lin}(0, CV_{\lambda,lin})$ and $\zeta_s(0, \sigma_{bd})$,

$$\rho_{exp} = \frac{\ln(2)(\sigma_x^2(2\alpha - 1)\alpha + \frac{\sigma_{bd}^2}{2})}{\langle \lambda \rangle \sigma_l \sigma_t}. \quad (66)$$

630 For the plot $\langle \lambda \rangle T_d$ vs $\ln(\frac{L_d}{L_b})$, the slope m_{lt} of the best linear fit is given by,

$$m_{lt} = \rho_{exp} \frac{\sigma_t \langle \lambda \rangle}{\sigma_l} = \frac{\ln(2)(\sigma_x^2(2\alpha - 1)\alpha + \frac{\sigma_{bd}^2}{2})}{\sigma_l^2}. \quad (67)$$

631 Inserting Equation 64 into Equation 67 and using Equation 57, we get,

$$m_{lt} = \frac{3}{2} \ln(2) \approx 1.0397. \quad (68)$$

632 Similarly the intercept (c_{lt}) for the plot $\langle \lambda \rangle T_d$ vs $\ln(\frac{L_d}{L_b})$ is found to be,

$$c_{lt} = \langle \langle \lambda \rangle T_d \rangle - m_{lt} \langle \ln(\frac{L_d}{L_b}) \rangle = \ln(2)(1 - \frac{3}{2} \ln(2)) \approx -0.0275. \quad (69)$$

633 This is very close to y=x trend obtained for the same regulatory mechanism controlling
634 division in exponentially growing cells (Figure 3A).

635 5.7 Growth rate vs age and elongation speed vs age plots.

636 In the previous sections, we found that binning and linear regression on the plot $\ln(\frac{L_d}{L_b})$ vs
637 $\langle \lambda \rangle T_d$, and the plot obtained by interchanging the axes, were inadequate to identify the mode

638 of growth. In this section, we try to validate the growth rate vs age plot as a method to
639 elucidate the mode of growth.

640 In addition to cell size at birth and division and the generation time, cell size trajectories
641 (cell size, L vs time from birth, t) were obtained for multiple cell cycles. In our case, the cell
642 size trajectories were collected either via simulations (in Figure 3B) or from experiments (for
643 Figures 4A-4C) at intervals of 4 min. For each trajectory, growth rate at time t or age $\frac{t}{T_d}$
644 is calculated as $\frac{1}{L(t)} \frac{L(t+\Delta t) - L(t)}{\Delta t}$ where Δt is the time between consecutive measurements. To
645 obtain elongation speed vs age plots, the formula before needs to be replaced with $\frac{L(t+\Delta t) - L(t)}{\Delta t}$.
646 The growth rate is interpolated to contain 200 points at equal intervals of time for each cell
647 trajectory. The growth rate trends appear to be robust with regards to a different number of
648 interpolated points (from 100 to 500 points). To obtain the growth rate trend as a function
649 of cell age, we use the method previously applied in Ref. [39]. In this method, growth rate is
650 binned based on age for each individual trajectory (50 bins) and the average growth rate is
651 obtained in each of the bins. The binned data trend for growth rate vs age is then found by
652 taking the average of the growth rate in each bin over all trajectories. Binning the growth
653 rate for each trajectory ensures that each trajectory has an equal contribution to the final
654 growth rate trend so as to avoid inspection bias. This step is especially important when data
655 collected at equal intervals of time is analyzed. In such a case, cells with larger generation
656 times have a greater number of measurements than cells with smaller generation times.
657 Obtaining the growth rate trend without binning growth rate for each trajectory would have
658 biased the binned data trend for the growth rate vs age plot to a smaller value because
659 of over-representation by slower-growing cells (or equivalently cells with longer generation
660 time). This bias towards lower growth rate values in the growth rate vs age plots is an
661 instance of inspection bias.

662 In Figures 4A-4C, we find the growth rate obtained from *E. coli* experiments to change
663 within the cell cycle. In the two slower growth media (Figures 4A, 4B), the growth rate is

664 found to increase with cell age while for the fastest growth media (Figure 4C) the growth
665 rate follows a non-monotonic behaviour similar to that observed in Ref. [39] for *B. subtilis*.
666 Abrupt changes in growth rate are reported at constriction in Refs. [41, 42]. We find that the
667 growth rate changes start before constriction in the two slower growth conditions considered.
668 One possibility is that this increase is due to preseptal cell wall synthesis [56]. Preseptal cell
669 wall synthesis does not require activity of PBP3 (FtsI) but instead relies on bifunctional
670 glycosyltransferases PBP1A and PBP1B that link to FtsZ via ZipA. One hypothesis that
671 can be tested in future works is that at the onset of constriction, activity from PBP1A
672 and PBP1B starts to gradually shift to the PBP3/FtsW complex and therefore no abrupt
673 change in growth rate is observed. In the fastest growth condition (glucose-cas medium), we
674 find that the increase in growth rate approximately coincides with onset of constriction, in
675 agreement with the previous findings [41, 42].

676 In Figures 4A-4C, the growth rate trends are not obtained for age close to one. This
677 is because growth rate at age = 1 is given by $\frac{1}{L(T_d)} \frac{L(T_d + \Delta t) - L(T_d)}{\Delta t}$ and this requires knowing
678 the cell lengths beyond the division event ($L(T_d + \Delta t)$). To estimate growth rates at age
679 close to one, we approximate $L(T_d + \Delta t)$ to be the sum of cell sizes of the two daughter
680 cells. In order to minimize inspection bias, we considered only those cell size trajectories
681 which had $L(t)$ data for 12 min after division (corresponding to an age of approximately
682 1.1). However, the growth rate trends in all three growth media were robust with regards to
683 a different time for which $L(t)$ was considered (4 min to 20 min after division). We use the
684 binning procedure discussed before in this section. To validate this method, we applied it
685 on synthetic data obtained from the simulations of exponentially growing cells following the
686 adder and the adder per origin model. Cells were assumed to divide in a perfectly symmetric
687 manner and both of the daughter cells were assumed to grow with the same growth rate,
688 independent of the growth rate in the mother cell. The growth rate trends for the two
689 models considered (adder and adder per origin) are expected to be constant even for cell age

690 > 1 . We found that the growth rate trends were indeed approximately constant as shown in
691 Figure 4- figure supplement 1D. We also considered linear growth with division controlled via
692 an adder model. The daughter cells were assumed to grow with the same elongation speed,
693 independent of the elongation speed in the mother cell. In this case, we expect the elongation
694 speed trend to be constant for cell age > 1 . This is indeed what we observed as shown in the
695 inset of Figure 4- figure supplement 1D. We used this method on *E. coli* experimental data
696 and found that the growth rate trends obtained for the three growth conditions (Figure 4-
697 figure supplements 1A-1C) were consistent with that shown in Figures 4A-4C in the relevant
698 age ranges. For cell age close to one, we found that the growth rate decreased to a value
699 close to the growth rate near cell birth (age ≈ 0) for all three growth conditions considered.

700 In summary, we find that the growth rate vs age plots are a consistent method to probe
701 the mode of cell growth within a cell cycle.

702 5.8 Growth rate vs time from specific event plots are affected by 703 inspection bias

704 To probe the growth rate trend in relation to a specific cell cycle event, for example cell birth,
705 growth rate vs time from birth plots are obtained for simulations of exponentially growing
706 cells following the adder model. In the growth rate vs time from birth plot, the rate is found
707 to stay constant and then decrease at longer times (Figure 3- figure supplement 2C) even
708 though cells are exponentially growing. Because of inspection bias (or survivor bias), at later
709 times, only the cells with larger generation times (or slower growth rates) “survive”. The
710 average generation time of the cells averaged upon in each bin of Figure 3- figure supplement
711 2C is shown in Figure 3- figure supplement 2D. The decrease in growth rate in Figure 3-
712 figure supplement 2C occurs around the same time when an increase in generation time is
713 observed in Figure 3- figure supplement 2D. Thus, the trend in growth rate is biased towards

714 lower values at longer times. The problem might be circumvented by restricting the time on
715 the x-axis to the smallest generation time of all the cell cycles considered [31].

716 To check for growth rate changes at constriction, we used plots of growth rate vs time
717 from constriction ($t - T_n$). Growth rate trends obtained from *E. coli* experimental data show
718 a decrease at the edges of the plots (Figure 4- figure supplements 2A, 2C, and 2E). These
719 deviate from the trends obtained using the growth rate vs age plots (Figures 4A-4C). To
720 investigate this discrepancy, we use a model which takes into account the constriction and
721 the division event. Currently it is unknown how constriction is related to division. For the
722 purpose of methods validation, we use a model where cells grow exponentially, constriction
723 occurs after a constant size addition from birth, and division occurs after a constant size
724 addition from constriction. Note that other models where constriction occurs after a constant
725 size addition from birth while division occurs after a constant time from constriction, as well
726 as a mixed timer-adder model proposed in Ref. [42], lead to similar results. We expect the
727 growth rate trend to be constant for exponentially growing cells. However, we find using
728 numerical simulations that it decreases at the plot edges both before and after the constriction
729 event (Figure 3- figure supplement 2A). This decrease can be attributed to inspection bias.
730 The average growth rate in time bins at the extremes are biased by cells with smaller growth
731 rates. This is shown in Figure 3- figure supplement 2B where the average generation time
732 for the cells contributing in each of the bins of Figure 3- figure supplement 2A is plotted.
733 The time at which the growth rate decreases on both sides of the constriction event is close
734 to the time at which the average generation time increases. For example, in alanine medium,
735 the generation time for each of the bins is plotted in Figure 4- figure supplement 2B. The
736 average generation time for the cells contributing to each of the bins is almost constant for
737 the timings between -80 min to 20 min. Thus, for this time range the changes in growth rate
738 are not because of inspection bias but are a real biological effect. The behavior of growth
739 rate within this time range in Figure 4- figure supplement 2A is in agreement with the trend

740 in growth rate vs age plot of Figure 4A. On accounting for inspection bias, the growth rate
741 vs age plots agree with the growth rate vs time from constriction plots in other growth media
742 as well (Figure 4- figure supplement 2C, Figure 4- figure supplement 2E). Thus, growth rate
743 vs time plots are also a consistent method to probe growth rate modulation in the time range
744 when avoiding the regimes prone to inspection bias.

745 5.9 Results of elongation speed vs size plots are model-dependent.

746 Cells assumed to undergo exponential growth have elongation speed proportional to their
747 size. In the case of exponential growth, the binned data trend of the plot elongation speed vs
748 size is expected to be linear with the slope of the best linear fit providing the value of growth
749 rate and intercept being zero. In this section, we use the simulations to test if binning and
750 linear regression on the elongation speed vs size plots are suitable methods to differentiate
751 exponential growth from linear growth [43].

752 To test the method, we generate cell size trajectories using simulations of the adder model
753 with a size additive division timing noise and assuming exponential growth. Elongation speed
754 at size $L(t)$ is calculated for each trajectory as $\frac{L(t+\Delta t)-L(t)}{\Delta t}$ where Δt is the time between
755 consecutive measurements ($= 4$ min in our case). Each trajectory is binned into 10 equally
756 sized bins based on their cell sizes and the average elongation speed is obtained for each bin.
757 The final trend of elongation speed as a function of size is then obtained by binning (based
758 on size) the pooled average elongation speed data of all the cell cycles.

759 We find that the binned data trend is linear with the slope of the best linear fit close to the
760 average growth rate considered in the simulations (Figure 3- figure supplement 3D). This is
761 in agreement with our expectations for exponential growth. In order to check if this method
762 could differentiate between exponential growth and linear growth, we used simulations of
763 the adder model undergoing linear growth to generate cell size trajectories for multiple cell
764 cycles. For linear growth, elongation speed is expected to be constant, independent of its

765 cell size. The binned data trend for the elongation speed vs size plot is also obtained to be
766 constant for the simulations of linearly growing cells (Figure 3- figure supplement 3B). The
767 intercept of the best linear fit obtained is close to the average elongation speed considered in
768 the simulations. The binned data trend for linear and exponential growth are clearly different
769 as shown in Figure 3- figure supplement 3B and Figure 3- figure supplement 3D, respectively,
770 and this result holds for a broad class of models where the division event is controlled by
771 birth and the growth rate (for exponential growth)/elongation speed (for linear growth) is
772 distributed normally and independently between cell-cycles.

773 Next, we consider the adder per origin cell cycle model for exponentially growing cells
774 [17]. In this model space, the cell initiates DNA replication by adding a constant size per
775 origin from the previous initiation size. The division occurs on average after a constant time
776 from initiation. For exponentially growing cells, the binned data trend is still expected to be
777 linear as before. Instead, we find using simulations that the trend is non-linear and it might
778 be misinterpreted as non-exponential growth (Figure 3- figure supplement 3F).

779 Thus, the results of binning and linear regression for the plot elongation speed vs size is
780 model-dependent.

781 5.10 Interchanging axes in growth rate vs inverse generation time 782 plot might lead to different interpretations.

783 So far, our discussion was focused on the question of mode of single-cell growth. A related
784 problem regards the relation between growth rate (λ) and the inverse generation time ($\frac{1}{T_d}$).
785 On a population level, the two are clearly proportional to each other. However, single-cell
786 studies based on binning showed an intriguing non-linear dependence between the two, with
787 the two variables becoming uncorrelated in the faster-growth media. [25, 57]. Within the
788 same medium, the binned data curve for the plot λ vs $\frac{1}{T_d}$ flattened out for faster dividing

789 cells. The trend in the binned data was different from the trend of $y = \ln(2)x$ line as observed
790 for the population means. A priori one might speculate that the flattening in faster dividing
791 cells could be because the faster dividing cells might have less time to adapt their division
792 rate to transient fluctuations in the environment. Kennard *et al.* [57] insightfully also plotted
793 $\frac{1}{T_d}$ vs λ and found a collapse of the binned data for all growth conditions onto the $y = \ln(2)x$
794 line. These results are reminiscent of what we previously showed for the relation of $\ln(\frac{L_d}{L_b})$
795 and $\langle \lambda \rangle T_d$.

796 In the following, we will elucidate why this occurs in this case using an underlying model
797 and predicting the trend based on it. We use simulations of the adder model undergoing
798 exponential growth. The parameters for size added in a cell cycle and mean growth rates
799 are extracted from the experimental data. CV of growth rate is assumed lower in faster-
800 growth media as observed by Kennard *et al.* Using this model, we could obtain the same
801 pattern of flattening at faster-growth conditions that is observed in the experiments (Figure
802 2- figure supplement 2A). The population mean for λ and $\frac{1}{T_d}$ follows the expected $y = \ln(2)x$
803 equation (shown as black dashed line) as was the case in experiments. Intuitively, such a
804 departure from the expected $y = \ln(2)x$ line for the single cell data can again be explained by
805 determining the effect of noise on variables plotted on both axes. As previously stated T_d is
806 affected by both growth rate noise and noise in division timing while growth rate fluctuates
807 independently of other sources of noise. This does not agree with the assumption for binning
808 as noise in division timing affects the x-axis variable rather than the y-axis variable. In such
809 a case, the trend in the binned data might not follow the expected $y = \ln(2)x$ line. However,
810 on interchanging the axes, we would expect the assumptions of binning to be met and the
811 trend to follow the $y = \frac{1}{\ln(2)}x$ line (Figure 2- figure supplement 2B).

812 5.11 Data and simulations

813 5.11.1 Experimental data

814 Experimental data obtained by Tanouchi *et al.* [10] was used to plot L_d vs L_b shown in
815 Figure 1A. *E. coli* cells were grown at 25°C in a mother machine device and the length at
816 birth and division were collected for multiple cell cycles. L_d vs L_b plot was obtained using
817 these cells and linear regression performed on it provided a best linear fit.

818 Data from recent mother machine experiments on *E. coli* was used to make all other
819 plots. Details are provided in Section 5.1 and Ref. [32]. The experiments were conducted at
820 28°C in three different growth conditions - alanine, glycerol and glucose-cas (also see Section
821 5.1). Cell size trajectories were collected for multiple cell cycles and all of the data collected
822 were considered while making the plots in the paper.

823 5.11.2 Simulations

824 MATLAB R2021a was used for simulations. Simulations of the adder model for exponentially
825 growing cells were carried out over a single lineage of 2500 generations (Figures 2C, 2D,
826 Figure 3- figure supplement 1C). The mean length added between birth and division was
827 set to 1.73 μm in line with the experimental results for alanine medium. Growth rate was
828 variable and sampled from a normal distribution at the start of each cell cycle. The mean
829 growth rate was set to $\frac{\ln(2)}{\langle T_d \rangle}$, where $\langle T_d \rangle = 212$ min and coefficient of variation (CV) = CV_λ
830 = 0.15. The noise in division timing was assumed to be time additive with mean 0 and
831 standard deviation $\frac{\sigma_n}{\langle \lambda \rangle}$, where $\sigma_n = 0.15$. The binning data trends and the best linear fits
832 obtained using these simulations could be compared with the analytical results obtained in
833 Sections 5.4.2 and 5.6.

834 For simulations of linear growth (Figures 3A-3B, Figure 3- figure supplements 1A, 1B, 3A,
835 3B, Figure 4- figure supplement 1D), the mean growth rate was set to $\frac{\langle L_d - L_b \rangle}{\langle T_d \rangle}$, with the values

836 of $\langle L_d - L_b \rangle$ and $\langle T_d \rangle$ used as mentioned previously. The noise in division timing was size
837 additive with standard deviation = $0.15\langle L_b \rangle$. Noise was also considered to be size additive
838 with the same standard deviation for the simulations of exponentially growing cells shown
839 in Figure 3B, Figure 3- figure supplements 2C, 3C, 3D, and Figure 4- figure supplement 1D.

840 For Figure 3B, Figure 3- figure supplements 3E, 3F, Figure 4- figure supplement 1D,
841 simulations were carried out over a lineage of 2500 generations for exponentially growing cells
842 following the adder per origin model. In the simulations, the time increment is 0.01 min.
843 The initial condition for the simulations is that cells are born and initiate DNA replication
844 at time $t=0$ but the results are independent of initial conditions. The number of origins is
845 also tracked throughout the simulations beginning with an initial value of 2. Cells divide
846 into two daughter cells in a perfectly symmetrical manner (no noise in division ratio), and
847 one of the daughter cells is discarded for the next cell cycle. In simulations, the growth rate
848 was fixed within a cell cycle but varied between different cell cycles. On division, the growth
849 rate for that cell cycle was drawn from a normal distribution with mean $\langle \lambda \rangle$ and coefficient of
850 variation (CV_λ) whose values were fixed using the experimental data from alanine medium.
851 The total length at which the next initiation happens is determined by,

$$L_i^{tot,next} = L_i + O\Delta_{ii}, \quad (70)$$

852 where Δ_{ii} is the length added per origin and O is the number of origins. To determine
853 $L_i^{tot,next}$, Δ_{ii} was drawn on reaching initiation length from a normal distribution. The mean
854 and CV of Δ_{ii} was obtained from experiments done in alanine medium. In the adder per
855 origin model, division happens after a C+D time from initiation. The division length (L_d)
856 is obtained to be,

$$L_d = L_i e^{\lambda(C+D)}. \quad (71)$$

857 In the simulations, once the initiation length was reached, the corresponding division oc-

858 curred a time C+D after initiation. C+D timings for each initiation event were again drawn
859 from a normal distribution with the same mean and CV as that of the experiments in alanine
860 medium.

861 For Figure 3- figure supplement 2A, cells were assumed to grow exponentially in the
862 simulations. The constriction length (L_n) was set to be,

$$L_n = L_b + \Delta_{bn}. \quad (72)$$

863 The length added (Δ_{bn}) was assumed to have a normal distribution with the mean length
864 added between birth and constriction set to $1.18 \mu m$ and the $CV = 0.23$, in line with the
865 experimental results for alanine medium. The length at division was set as,

$$L_d = L_n + \Delta_{nd}. \quad (73)$$

866 The length added (Δ_{nd}) was also assumed to have a normal distribution with the mean
867 length added set to $0.53 \mu m$ and the $CV = 0.26$, again in line with the experimental results
868 for alanine medium.

869 For Figure 3B, Figure 3- figure supplements 2A-2D, 3A-3F, Figure 4- figure supplement
870 1D, the cell sizes are recorded within the cell cycle at equal intervals of 4 min, similar to
871 that in the *E. coli* experiments of Ref. [32].

872 For simulations shown in Figure 4- figure supplement 1D, the cell size trajectories are
873 obtained at intervals of 4 min beyond the current cell-cycle. The size after the division event
874 is said to be the sum of the sizes of the daughter cells. It is also further assumed that
875 the daughter cells are equal in size (perfectly symmetric division) and they both grow with
876 the same growth rate (for exponential growth) or elongation speed (for linear growth). The
877 growth rates/elongation speeds for the daughter cells are sampled from a normal distribution
878 with a mean and CV as discussed before. The cell size trajectories are recorded for 80 min

879 after the division event in the current cell cycle.

880 In Figure 2- figure supplement 2, simulations of the adder model for exponentially growing
881 cells were carried out until a population of 5000 cells was reached. The parameters for size
882 added in a cell cycle and mean growth rates were extracted from the experimental data [57].
883 The value of σ_n used in all growth conditions was 0.17 while CV_λ decreased in faster growth
884 conditions (0.2 in the three slowest growth conditions, 0.12 and 0.07 in the second fastest
885 and fastest growth conditions respectively).

886 6 Acknowledgements

887 The authors thank Ethan Levien, Jie Lin for useful discussions, Jane Kondev, Xili Liu, and
888 Marco Cosentino Lagomarsino for their useful feedback on the manuscript, Da Yang and
889 Scott Retterer for help in microfluidic chip making, and Rodrigo Reyes-Lamothe for a kind
890 gift of strain. Authors acknowledge technical assistance and material support from the Center
891 for Environmental Biotechnology at the University of Tennessee. A part of this research was
892 conducted at the Center for Nanophase Materials Sciences, which is sponsored at Oak Ridge
893 National Laboratory by the Scientific User Facilities Division, Office of Basic Energy Sciences,
894 U.S. Department of Energy. This work has been supported by the US-Israel BSF research
895 grant 2017004 (JM), the National Institutes of Health award under R01GM127413 (JM),
896 NSF CAREER 1752024 (AA), NIH grant 103346 (PK) and NSF award 1806818 (PK).

897 7 Conflict of interest

898 The authors declare that they have no conflicts of interest with the contents of this article.

899 References

- 900 1. Osella, M., Tans, S.J., and Lagomarsino, M.C. (2017). Step by Step, Cell by Cell: Quantification of the Bacterial Cell Cycle. *Trends in Microbiology* *25*, 250–256.
- 902 2. Facchetti, G., Chang, F., and Howard, M. (2017). Controlling cell size through sizer mechanisms. *Current Opinion in Systems Biology* *5*, 86–92.
- 904 3. Ho, P.Y., Lin, J., and Amir, A. (2018). Modeling cell size regulation: From single-cell-level statistics to molecular mechanisms and population-level effects. *Annual Review of Biophysics* *47*, 251–271.
- 907 4. Soifer, I., Robert, L., and Amir, A. (2016). Single-cell analysis of growth in budding yeast and bacteria reveals a common size regulation strategy. *Current Biology* *26*, 356–361.
- 909 5. Jun, S., Si, F., Pugatch, R., and Scott, M. (2018). Fundamental principles in bacterial physiology—history, recent progress, and the future with focus on cell size control: a review. *Reports on Progress in Physics* *81*, 056601.
- 912 6. Amir, A. and Balaban, N.Q. (2018). Learning from noise: how observing stochasticity may aid microbiology. *Trends in Microbiology* *26*, 376–385.
- 914 7. Kohram, M., Vashistha, H., Leibler, S., Xue, B., and Salman, H. (2021). Bacterial growth control mechanisms inferred from multivariate statistical analysis of single-cell measurements. *Current Biology* *31*, 955–964.
- 917 8. Hogg, D.W., Bovy, J., and Lang, D. (2010). Data analysis recipes: Fitting a model to data. *arXiv preprint arXiv:1008.4686* .
- 919 9. Kiviet, D.J., Nghe, P., Walker, N., Boulineau, S., Sunderlikova, V., and Tans, S.J. (2014). Stochasticity of metabolism and growth at the single-cell level. *Nature* *514*, 376–379.

921 10. Tanouchi, Y., Pai, A., Park, H., Huang, S., Buchler, N.E., and You, L. (2017). Long-term
922 growth data of *Escherichia coli* at a single-cell level. *Scientific Data* *4*, 1–5.

923 11. Harris, L.K. and Theriot, J.A. (2016). Relative rates of surface and volume synthesis set
924 bacterial cell size. *Cell* *165*, 1479–1492.

925 12. Si, F., Le Treut, G., Sauls, J.T., Vadia, S., Levin, P.A., and Jun, S. (2019). Mechanistic
926 origin of cell-size control and homeostasis in bacteria. *Current Biology* *29*, 1760–1770.

927 13. Amir, A. (2014). Cell size regulation in bacteria. *Physical Review Letters* *112*, 208102.

928 14. Campos, M., Surovtsev, I.V., Kato, S., Paintdakhi, A., Beltran, B., Ebmeier, S.E., and
929 Jacobs-Wagner, C. (2014). A constant size extension drives bacterial cell size homeosta-
930 sis. *Cell* *159*, 1433–1446.

931 15. Taheri-Araghi, S., Bradde, S., Sauls, J.T., Hill, N.S., Levin, P.A., Paulsson, J., Vergas-
932 sola, M., and Jun, S. (2015). Cell-size control and homeostasis in bacteria. *Current
933 Biology* *25*, 385–391.

934 16. Eun, Y.J., Ho, P.Y., Kim, M., LaRussa, S., Robert, L., Renner, L.D., Schmid, A.,
935 Garner, E., and Amir, A. (2018). Archaeal cells share common size control with bacteria
936 despite noisier growth and division. *Nature Microbiology* *3*, 148–154.

937 17. Ho, P.Y. and Amir, A. (2015). Simultaneous regulation of cell size and chromosome
938 replication in bacteria. *Frontiers in Microbiology* *6*, 662.

939 18. Micali, G., Grilli, J., Osella, M., and Lagomarsino, M.C. (2018). Concurrent processes
940 set *E. coli* cell division. *Science Advances* *4*, eaau3324.

941 19. Witz, G., van Nimwegen, E., and Julou, T. (2019). Initiation of chromosome repli-
942 cation controls both division and replication cycles in *E. coli* through a double-adder
943 mechanism. *eLife* *8*, e48063.

944 20. Barber, F., Ho, P.Y., Murray, A.W., and Amir, A. (2017). Details matter: noise and
945 model structure set the relationship between cell size and cell cycle timing. *Frontiers in*
946 *Cell and Developmental Biology* *5*, 92.

947 21. Facchetti, G., Knapp, B., Chang, F., and Howard, M. (2019). Reassessment of the basis
948 of cell size control based on analysis of cell-to-cell variability. *Biophysical Journal* *117*,
949 1728–1738.

950 22. Godin, M., Delgado, F.F., Son, S., Grover, W.H., Bryan, A.K., Tzur, A., Jorgensen,
951 P., Payer, K., Grossman, A.D., Kirschner, M.W., et al. (2010). Using buoyant mass to
952 measure the growth of single cells. *Nature Methods* *7*, 387–390.

953 23. Wang, P., Robert, L., Pelletier, J., Dang, W.L., Taddei, F., Wright, A., and Jun, S.
954 (2010). Robust growth of *Escherichia coli*. *Current Biology* *20*, 1099–1103.

955 24. Cermak, N., Olcum, S., Delgado, F.F., Wasserman, S.C., Payer, K.R., Murakami, M.A.,
956 Knudsen, S.M., Kimmerling, R.J., Stevens, M.M., Kikuchi, Y., et al. (2016). High-
957 throughput measurement of single-cell growth rates using serial microfluidic mass sensor
958 arrays. *Nature Biotechnology* *34*, 1052–1059.

959 25. Iyer-Biswas, S., Wright, C.S., Henry, J.T., Lo, K., Burov, S., Lin, Y., Crooks, G.E.,
960 Crosson, S., Dinner, A.R., and Scherer, N.F. (2014). Scaling laws governing stochastic
961 growth and division of single bacterial cells. *Proceedings of the National Academy of
962 Sciences* *111*, 15912–15917.

963 26. Scott, M., Gunderson, C.W., Mateescu, E.M., Zhang, Z., and Hwa, T. (2010). Inter-
964 dependence of cell growth and gene expression: origins and consequences. *Science* *330*,
965 1099–1102.

966 27. Lin, J. and Amir, A. (2018). Homeostasis of protein and mRNA concentrations in
967 growing cells. *Nature Communications* *9*, 1–11.

968 28. Metzl-Raz, E., Kafri, M., Yaakov, G., Soifer, I., Gurvich, Y., and Barkai, N. (2017). Principles of cellular resource allocation revealed by condition-dependent proteome profiling.

969

970 eLife 6, e28034.

971 29. Kafri, M., Metzl-Raz, E., Jonas, F., and Barkai, N. (2016). Rethinking cell growth

972 models. FEMS Yeast Research 16.

973 30. Logsdon, M.M., Ho, P.Y., Papavinasasundaram, K., Richardson, K., Cokol, M., Sassetti,

974 C.M., Amir, A., and Aldridge, B.B. (2017). A parallel adder coordinates mycobacterial

975 cell-cycle progression and cell-size homeostasis in the context of asymmetric growth and

976 organization. Current Biology 27, 3367–3374.

977 31. Messelink, J., Meyer, F., Bramkamp, M., and Broedersz, C. (2020). Single-cell growth

978 inference of *Corynebacterium glutamicum* reveals asymptotically linear growth. bioRxiv,

979 10.1101/2020.05.25.115055 .

980 32. Tiruvadi Krishnan, S., Männik, J., Kar, P., Lin, J., Amir, A., and Männik, J. (2021).
981 Replication-related control over cell division in *Escherichia coli* is growth-rate dependent.
982 bioRxiv, 10.1101/2021.02.18.431686 .

983 33. Furchtgott, L., Wingreen, N.S., and Huang, K.C. (2011). Mechanisms for maintaining

984 cell shape in rod-shaped Gram-negative bacteria. Molecular Microbiology 81, 340–353.

985 34. Adiciptaningrum, A., Osella, M., Moolman, M.C., Lagomarsino, M.C., and Tans, S.J.
986 (2015). Stochasticity and homeostasis in the *E. coli* replication and division cycle.
987 Scientific Reports 5, 1–8.

988 35. Stein, W.E. and Dattero, R. (1985). Sampling bias and the inspection paradox. Mathematics Magazine 58, 96–99.

990 36. Mitchison, J. (2005). Single cell studies of the cell cycle and some models. *Theoretical
991 Biology and Medical Modelling* *2*, 4.

992 37. Abner, K., Aaviksaar, T., Adamberg, K., and Vilu, R. (2014). Single-cell model of
993 prokaryotic cell cycle. *Journal of Theoretical Biology* *341*, 78–87.

994 38. Deforet, M., Van Ditmarsch, D., and Xavier, J.B. (2015). Cell-size homeostasis and the
995 incremental rule in a bacterial pathogen. *Biophysical Journal* *109*, 521–528.

996 39. Nordholt, N., van Heerden, J.H., and Bruggeman, F.J. (2020). Biphasic cell-size and
997 growth-rate homeostasis by single *Bacillus subtilis* cells. *Current Biology* *30*, 2238–2247.

998 40. Knapp, B.D., Odermatt, P., Rojas, E.R., Cheng, W., He, X., Huang, K.C., and Chang, F.
999 (2019). Decoupling of rates of protein synthesis from cell expansion leads to supergrowth.
1000 *Cell Systems* *9*, 434–445.

1001 41. Reshes, G., Vanounou, S., Fishov, I., and Feingold, M. (2008). Cell shape dynamics in
1002 *Escherichia coli*. *Biophysical Journal* *94*, 251–264.

1003 42. Banerjee, S., Lo, K., Daddysman, M.K., Selewa, A., Kuntz, T., Dinner, A.R., and
1004 Scherer, N.F. (2017). Biphasic growth dynamics control cell division in *Caulobacter
1005 crescentus*. *Nature Microbiology* *2*, 1–6.

1006 43. Cadart, C., Venkova, L., Recho, P., Lagomarsino, M.C., and Piel, M. (2019). The physics
1007 of cell-size regulation across timescales. *Nature Physics* *15*, 993–1004.

1008 44. Panlilio, M., Grilli, J., Tallarico, G., Iuliani, I., Sclavi, B., Cicuta, P., and Lagomarsino,
1009 M.C. (2021). Threshold accumulation of a constitutive protein explains *E. coli* cell-
1010 division behavior in nutrient upshifts. *Proceedings of the National Academy of Sciences
1011* *118*.

1012 45. Willis, L. and Huang, K.C. (2017). Sizing up the bacterial cell cycle. *Nature Reviews Microbiology* *15*, 606–620.

1014 46. Simpson, E.H. (1951). The interpretation of interaction in contingency tables. *Journal of the Royal Statistical Society: Series B (Methodological)* *13*, 238–241.

1016 47. Aldridge, B.B., Fernandez-Suarez, M., Heller, D., Ambravaneswaran, V., Irimia, D.,
1017 Toner, M., and Fortune, S.M. (2012). Asymmetry and aging of mycobacterial cells lead
1018 to variable growth and antibiotic susceptibility. *Science* *335*, 100–104.

1019 48. Kubitschek, H. (1981). Bilinear cell growth of *Escherichia coli*. *Journal of Bacteriology*
1020 *148*, 730–733.

1021 49. Oldewurtel, E.R., Kitahara, Y., Cordier, B., Özbaykal, G., and van Teeffelen, S. (2019).
1022 Bacteria control cell volume by coupling cell-surface expansion to dry-mass growth.
1023 bioRxiv, <https://doi.org/10.1101/769786> .

1024 50. Datsenko, K.A. and Wanner, B.L. (2000). One-step inactivation of chromosomal genes
1025 in *Escherichia coli* K-12 using PCR products. *Proceedings of the National Academy of
1026 Sciences* *97*, 6640–6645.

1027 51. Thomason, L.C., Costantino, N., and Court, D.L. (2007). *E. coli* genome manipulation
1028 by P1 transduction. *Current Protocols in Molecular Biology* *79*, 1–17.

1029 52. Reyes-Lamothe, R., Sherratt, D.J., and Leake, M.C. (2010). Stoichiometry and archi-
1030 tecture of active DNA replication machinery in *Escherichia coli*. *Science* *328*, 498–501.

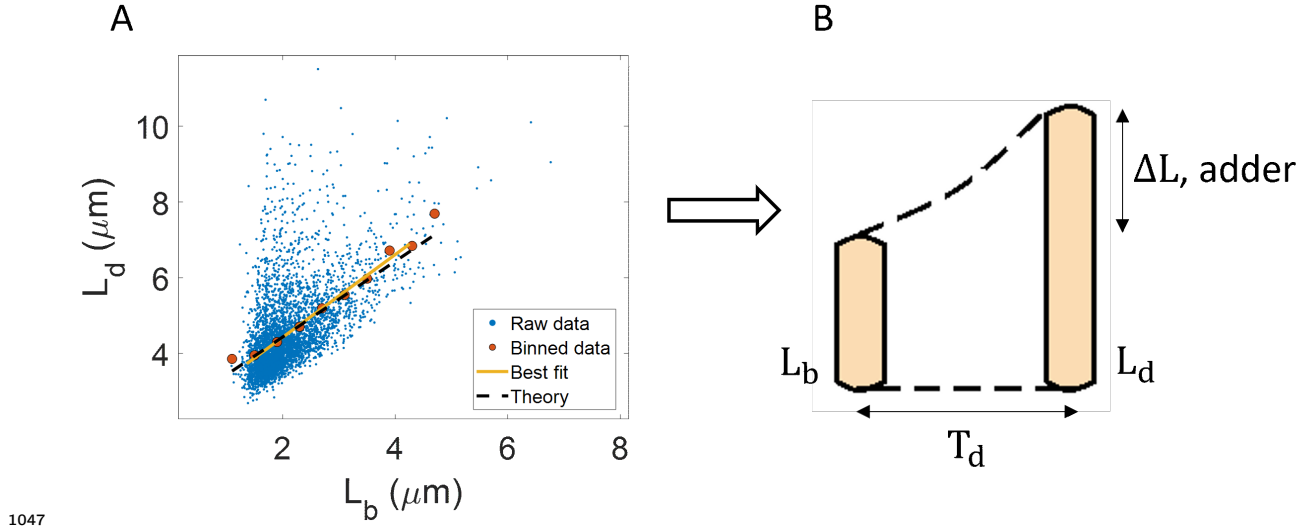
1031 53. Cherepanov, P.P. and Wackernagel, W. (1995). Gene disruption in *Escherichia coli*: TcR
1032 and KmR cassettes with the option of Flp-catalyzed excision of the antibiotic-resistance
1033 determinant. *Gene* *158*, 9–14.

1034 54. Moolman, M.C., Krishnan, S.T., Kerssemakers, J.W., Van Den Berg, A., Tulinski, P.,
1035 Depken, M., Reyes-Lamothe, R., Sherratt, D.J., and Dekker, N.H. (2014). Slow unloading
1036 leads to DNA-bound β 2-sliding clamp accumulation in live *Escherichia coli* cells.
1037 Nature Communications 5, 5820.

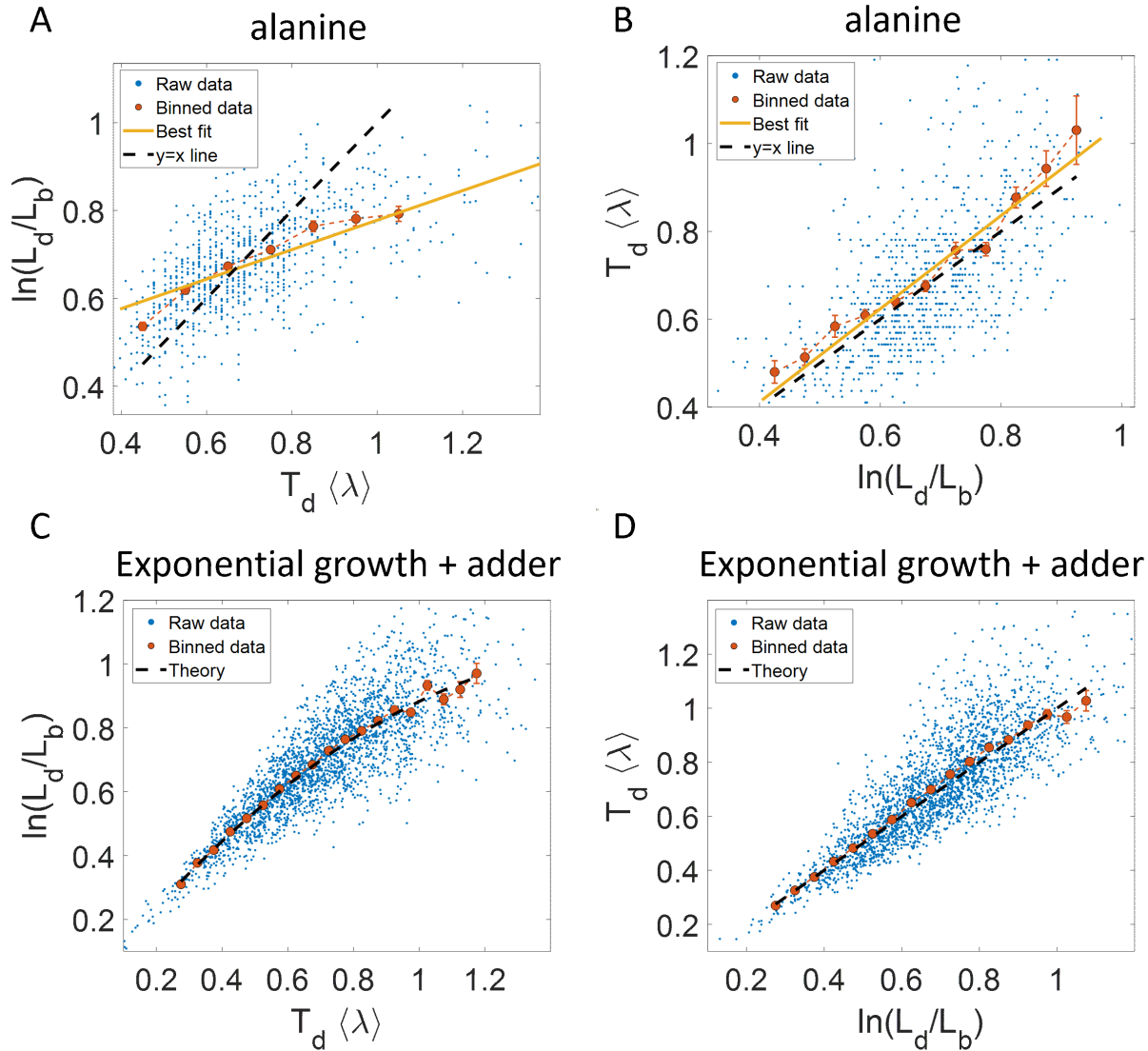
1038 55. Yang, D., Jennings, A.D., Borrego, E., Retterer, S.T., and Männik, J. (2018). Analysis
1039 of factors limiting bacterial growth in PDMS mother machine devices. Frontiers in
1040 Microbiology 9, 871.

1041 56. Pazos, M., Peters, K., Casanova, M., Palacios, P., VanNieuwenhze, M., Breukink, E.,
1042 Vicente, M., and Vollmer, W. (2018). Z-ring membrane anchors associate with cell wall
1043 synthases to initiate bacterial cell division. Nature Communications 9, 1–12.

1044 57. Kennard, A.S., Osella, M., Javer, A., Grilli, J., Nghe, P., Tans, S.J., Cicuta, P., and
1045 Lagomarsino, M.C. (2016). Individuality and universality in the growth-division laws of
1046 single *E. coli* cells. Physical Review E 93, 012408.

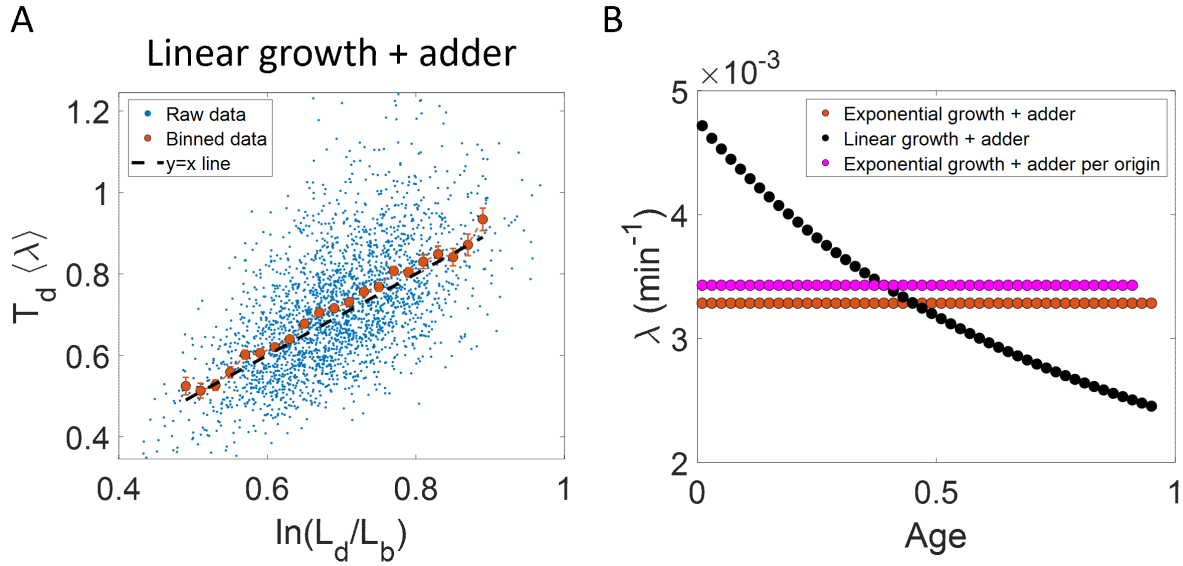


1047 Figure 1: **Utility of binning and linear regression:** **A.** Length at division (L_d) vs length
1048 at birth (L_b) is plotted using data obtained by Tanouchi *et al.* [10]. Raw data is shown as
1049 blue dots. We find the trend in binned data (red) to be linear with the underlying best
1050 fit (yellow) following the equation, $L_d = 1.09L_b + 2.24\mu m$. This is close to the adder
1051 behavior with an underlying equation given by $L_d = L_b + \Delta L$, where ΔL is the mean size
1052 added between birth and division (shown as black dashed line). **B.** A schematic of the adder
1053 mechanism is shown where the cell grows over its generation time (T_d) and divides after
1054 addition of length ΔL from birth. This ensures cell size homeostasis in single cells.
1055



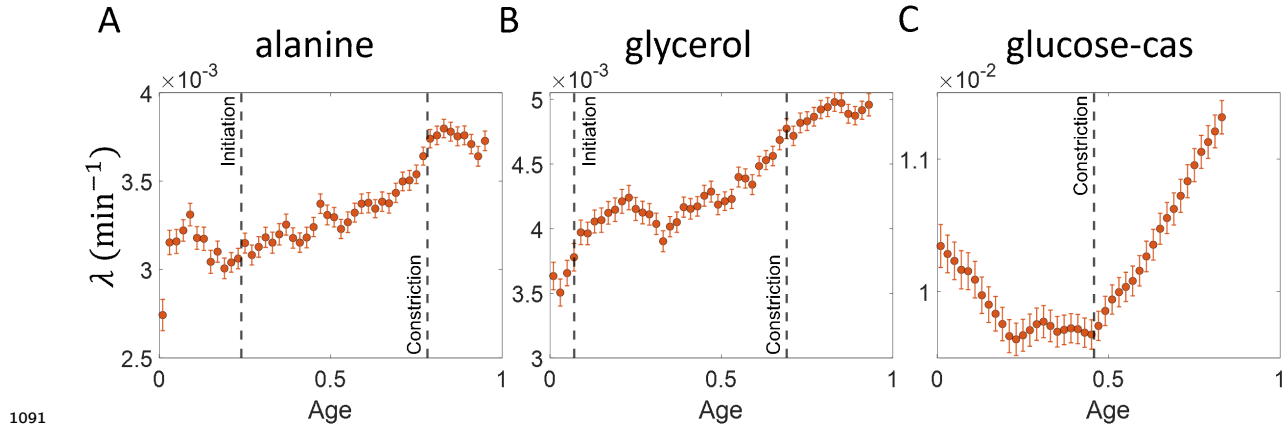
1057

Figure 2: **Plots that could potentially lead to misinterpreting exponential growth:**
 1058 **A, B.** Data is obtained from experiments in M9 alanine medium ($\langle T_d \rangle = 214$ min, $N = 816$ cells). **A.** $\ln(\frac{L_d}{L_b})$ vs $\langle \lambda \rangle T_d$ plot is shown. The blue dots are the raw data, the red correspond to the binned data trend, the yellow line is the best linear fit obtained by performing linear regression on the raw data and the black dashed line is the $y=x$ line. *A priori*, non-linear trend in binned data might point to growth being non-exponential. **B.** $\langle \lambda \rangle T_d$ vs $\ln(\frac{L_d}{L_b})$ plot is shown for the same experiments. **C, D.** Simulations of exponentially growing cells following the adder model are carried out for $N = 2500$ cells. The parameters used are provided in Section 5.11.2. **C.** $\ln(\frac{L_d}{L_b})$ vs $\langle \lambda \rangle T_d$ plot is shown. The trend in binned data shown in red is non-linear. The black dashed line is the expected trend obtained from theory (Equation 2). For parameters used in the simulations here, the black dashed line follows $\ln(\frac{L_d}{L_b}) = 1.26\langle \lambda \rangle T_d - 0.38(\langle \lambda \rangle T_d)^2$. **D.** $\langle \lambda \rangle T_d$ vs $\ln(\frac{L_d}{L_b})$ plot is shown with binned data in red closely following the expected trend of $y=x$ line (black dashed line). In all of these plots, the binned data is shown only for those bins with more than 15 data points in them.

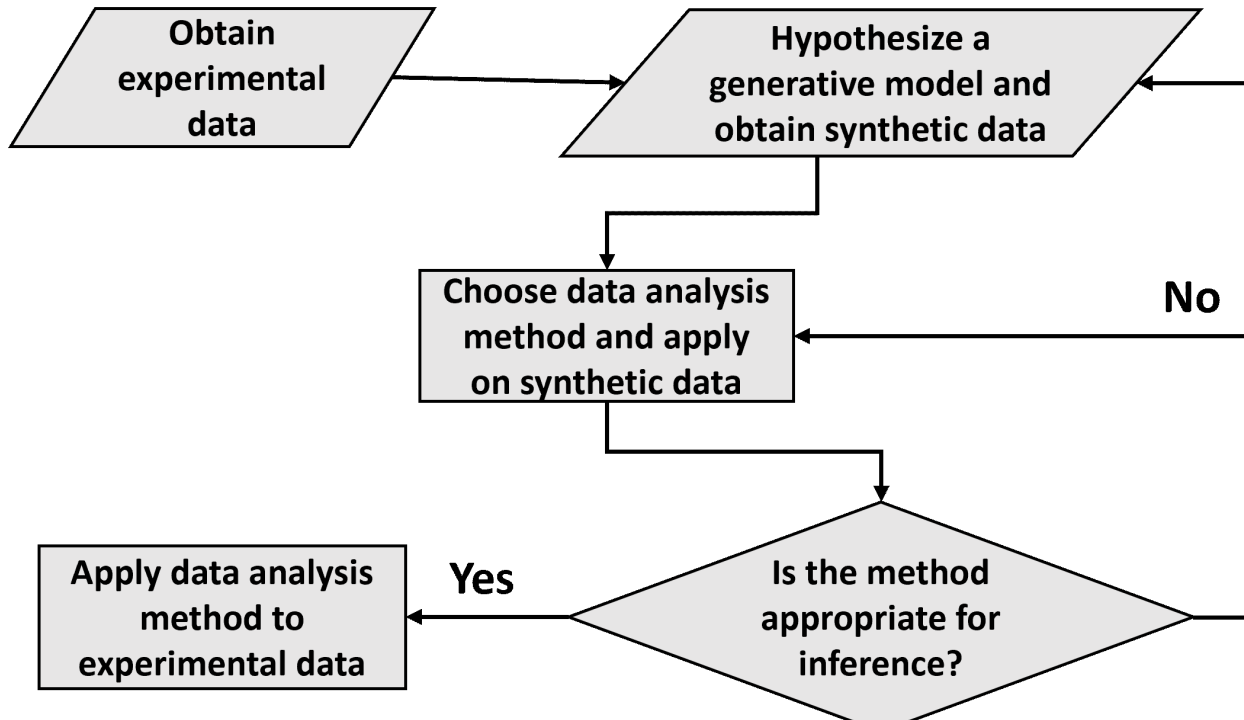


1073

1074 Figure 3: **Differentiating linear growth from exponential growth:** **A.** $\langle \lambda \rangle T_d$ vs $\ln(\frac{L_d}{L_b})$
 1075 plot is shown for simulations of linearly growing cells following the adder model for $N =$
 1076 2500 cell cycles. The binned data closely follows the $y=x$ trend which could be incorrectly
 1077 interpreted as cells undergoing exponential growth. **B.** The binned data trend for growth
 1078 rate vs age plot is shown in red for simulations of $N = 2500$ cell cycles of exponentially
 1079 growing cells following the adder model. We observe the trend to be nearly constant as
 1080 expected for exponential growth. Since the growth rate is fixed at the beginning of each cell
 1081 cycle in the above simulations, we do not show error bars for each bin within the cell cycle.
 1082 Also shown in black is the growth rate vs age plot for simulations of $N = 2500$ cell cycles of
 1083 linearly growing cells following the adder model. As expected for linear growth, the binned
 1084 growth rate decreases with age. The binned growth rate trend is also found to be nearly
 1085 constant for the simulations of exponentially growing cells following the adder per origin
 1086 model (shown in magenta). Thus, the plot growth rate vs age provides a consistent method
 1087 to identify the mode of growth. Parameters used in the above simulations of exponential
 1088 and linear growth are derived from the experimental data in alanine medium. Details are
 1089 provided in the Section 5.11.2.



1091 Figure 4: **Growth rate vs age obtained from experiments:** Growth rate vs age plots
 1092 are shown for *E. coli* experimental data. The red dots correspond to the binned data trends
 1093 showing the variation in growth rate. The medium in which the experiments were conducted
 1094 are **A.** Alanine ($\langle T_d \rangle = 214$ min) **B.** Glycerol ($\langle T_d \rangle = 164$ min) **C.** Glucose-cas ($\langle T_d \rangle = 65$
 1095 min). The error bars show the standard deviation of the growth rate in each bin scaled by
 1096 $\frac{1}{\sqrt{N}}$, where N is the number of cells in that bin. The dashed vertical lines mark the age at
 1097 initiation of DNA replication (left line) and the start of septum formation (right line). In
 1098 case of glucose-cas, the initiation age is not marked as it occurs in the mother cell.
 1099



1101

1102 Figure 5: A flowchart of the general framework proposed in the paper to carry out data
 1103 analysis.

1105 **8 Supplementary Figures and Tables**

Table S1: Variable definitions.

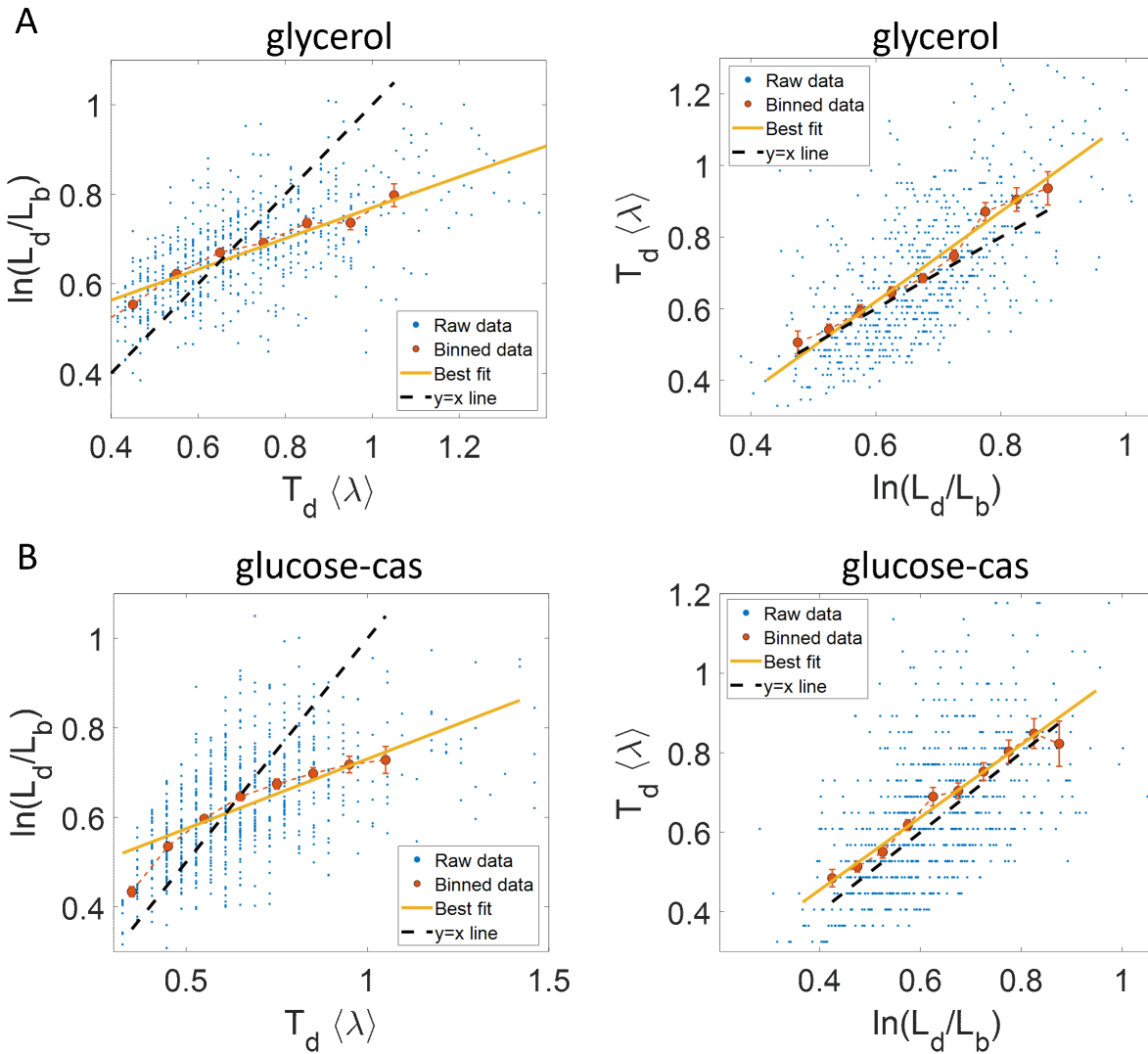
Variables	Description
L_b	Length of the cell at birth and also a proxy for size at birth
L_d	Length of the cell at division and also a proxy for size at division
l_b	$\frac{L_b}{\langle L_b \rangle}$, where $\langle L_b \rangle$ is mean size at birth
l_d	$\frac{L_d}{\langle L_b \rangle}$, where $\langle L_b \rangle$ is mean size at birth
$f(l_b)$	Mathematical function which captures the regulation strategy determining division given size at birth. $f(l_b) = 2l_b^{1-\alpha}$
T_d	Generation time
σ_t	Standard deviation of generation time
x_n or x	$x_n = \ln(l_b^n)$. Since $l_b \approx 1$, $x_n \approx l_b^n - 1$
σ_x	Standard deviation of x_n
$f_1(x_n)$	Gaussian describing the distribution of x_n . $f_1(x_n) = \frac{1}{\sqrt{2\pi\sigma_x^2}} \exp\left(-\frac{x_n^2}{2\sigma_x^2}\right)$
$\langle \lambda \rangle$	Mean growth rate
CV_λ	Coefficient of variation of growth rate
$\xi(0, CV_\lambda)$	Normally distributed growth rate noise. Growth rate is defined as $\lambda = \langle \lambda \rangle + \langle \lambda \rangle \xi(0, CV_\lambda)$
$f_2(\xi)$	Gaussian describing the distribution of random variable $\xi(0, CV_\lambda)$. $f_2(\xi) = \frac{1}{\sqrt{2\pi CV_\lambda^2}} \exp\left(-\frac{\xi^2}{2CV_\lambda^2}\right)$
$\frac{\xi(0, \sigma_n)}{\langle \lambda \rangle}$	Normally distributed time additive division timing noise with mean 0 and standard deviation $\frac{\sigma_n}{\langle \lambda \rangle}$

$f_3(\zeta)$	Gaussian describing the distribution of random variable $\zeta(0, \sigma_n)$. $f_3(\zeta) = \frac{1}{\sqrt{2\pi\sigma_n^2}} \exp\left(-\frac{\zeta^2}{2\sigma_n^2}\right)$
$\zeta_s(0, \sigma_{bd})$	Normally distributed size additive division timing noise with mean 0 and standard deviation σ_{bd}
σ_l	Standard deviation of $\ln(\frac{L_d}{L_b})$
$f_4\left(\ln\left(\frac{L_d}{L_b}\right)\right)$	Gaussian describing the distribution of $\ln(\frac{L_d}{L_b})$. $f_4\left(\ln\left(\frac{L_d}{L_b}\right)\right) = \frac{1}{\sqrt{2\pi\sigma_l^2}} \exp\left(-\frac{\left(\ln\left(\frac{L_d}{L_b}\right) - \ln(2)\right)^2}{2\sigma_l^2}\right)$
ρ_{exp}	Correlation coefficient of the pair $(\ln(\frac{L_d}{L_b}), \langle \lambda \rangle T_d)$
m_{tl}	Slope of the best linear fit for $\ln(\frac{L_d}{L_b})$ vs $\langle \lambda \rangle T_d$ plot
c_{tl}	Intercept of the best linear fit for $\ln(\frac{L_d}{L_b})$ vs $\langle \lambda \rangle T_d$ plot
m_{lt}	Slope of the best linear fit for $\langle \lambda \rangle T_d$ vs $\ln(\frac{L_d}{L_b})$ plot
c_{lt}	Intercept of the best linear fit for $\langle \lambda \rangle T_d$ vs $\ln(\frac{L_d}{L_b})$ plot
$\langle \lambda_{lin} \rangle$	Mean normalized elongation speed
$CV_{\lambda,lin}$	Coefficient of variation of normalized elongation speed
$\xi_{lin}(0, CV_{\lambda,lin})$	Normally distributed normalized elongation speed noise. Normalized elongation speed is defined as $\lambda_{lin} = \langle \lambda_{lin} \rangle + \langle \lambda_{lin} \rangle \xi_{lin}(0, CV_{\lambda,lin})$
$\sigma_{l,lin}$	Standard deviation of $l_d - l_b$
ρ_{lin}	Correlation coefficient of the pair $(l_d - l_b, \langle \lambda_{lin} \rangle T_d)$
$m_{tl,lin}$	Slope of the best linear fit for $l_d - l_b$ vs $\langle \lambda_{lin} \rangle T_d$ plot
$c_{tl,lin}$	Intercept of the best linear fit for $l_d - l_b$ vs $\langle \lambda_{lin} \rangle T_d$ plot
$m_{lt,lin}$	Slope of the best linear fit for $\langle \lambda_{lin} \rangle T_d$ vs $l_d - l_b$ plot
$c_{lt,lin}$	Intercept of the best linear fit for $\langle \lambda_{lin} \rangle T_d$ vs $l_d - l_b$ plot
L_i	Cell size at the start of DNA replication (initiation)

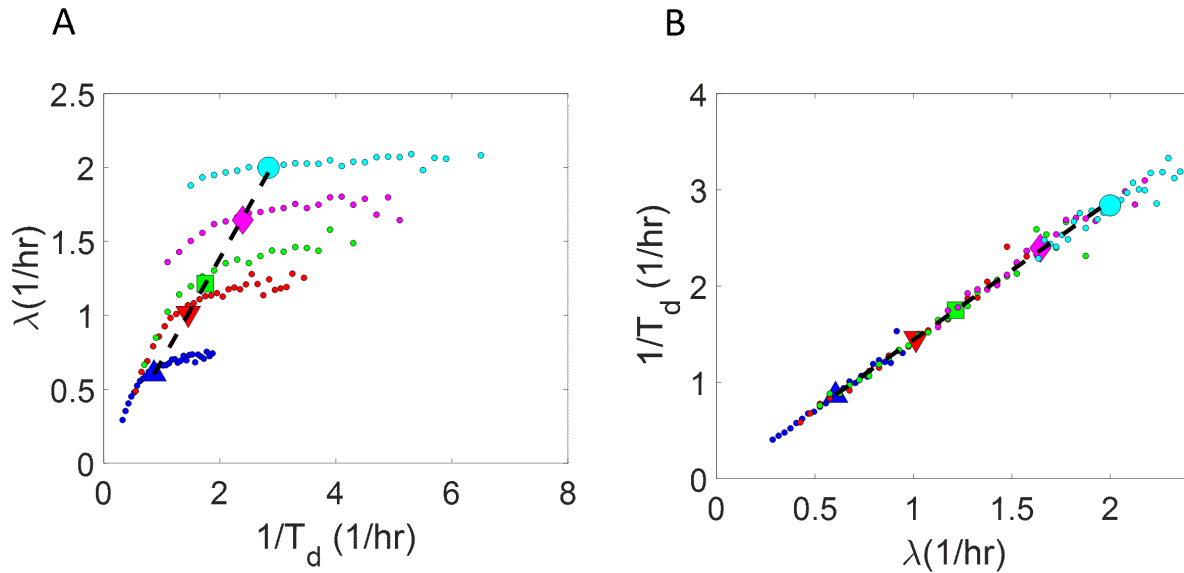
$L_i^{tot,next}$	Total cell size of the daughter cells at the start of DNA replication
Δ_{ii}	Size added per origin between initiations
O	Number of origins just after initiation
C+D	Time between initiation and division
T_n	Timing of start of septum formation/onset of constriction
L_n	Cell size at time T_n

Table S2: The slope and the intercept of the best linear fit along with their 95% confidence intervals (CI) obtained on performing linear regression on experimental data. The data is collected for cells growing in M9 alanine, glycerol and glucose-cas media [32].

Media	No. of cells	T_d (min)	$\ln(\frac{L_d}{L_b})$ vs $\langle \lambda \rangle T_d$ plot		$\langle \lambda \rangle T_d$ vs $\ln(\frac{L_d}{L_b})$ plot	
			Slope (with 95% CI)	Intercept (with 95% CI)	Slope (with 95% CI)	Intercept (with 95% CI)
Alanine	816	214	0.34 (0.31, 0.36)	0.44 (0.42, 0.46)	1.06 (0.98, 1.14)	-0.01 (-0.07, 0.04)
Glycerol	648	164	0.34 (0.32, 0.37)	0.43 (0.41, 0.44)	1.26 (1.16, 1.35)	-0.13 (-0.20, -0.07)
Glucose-cas	737	65	0.31 (0.28, 0.34)	0.42 (0.40, 0.44)	0.91 (0.83, 1.00)	0.09 (0.03, 0.15)

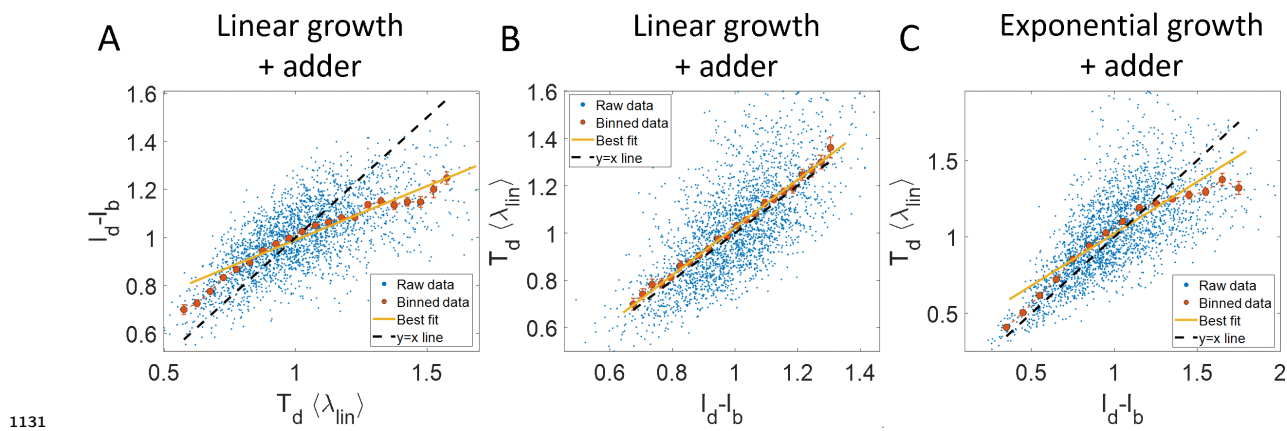


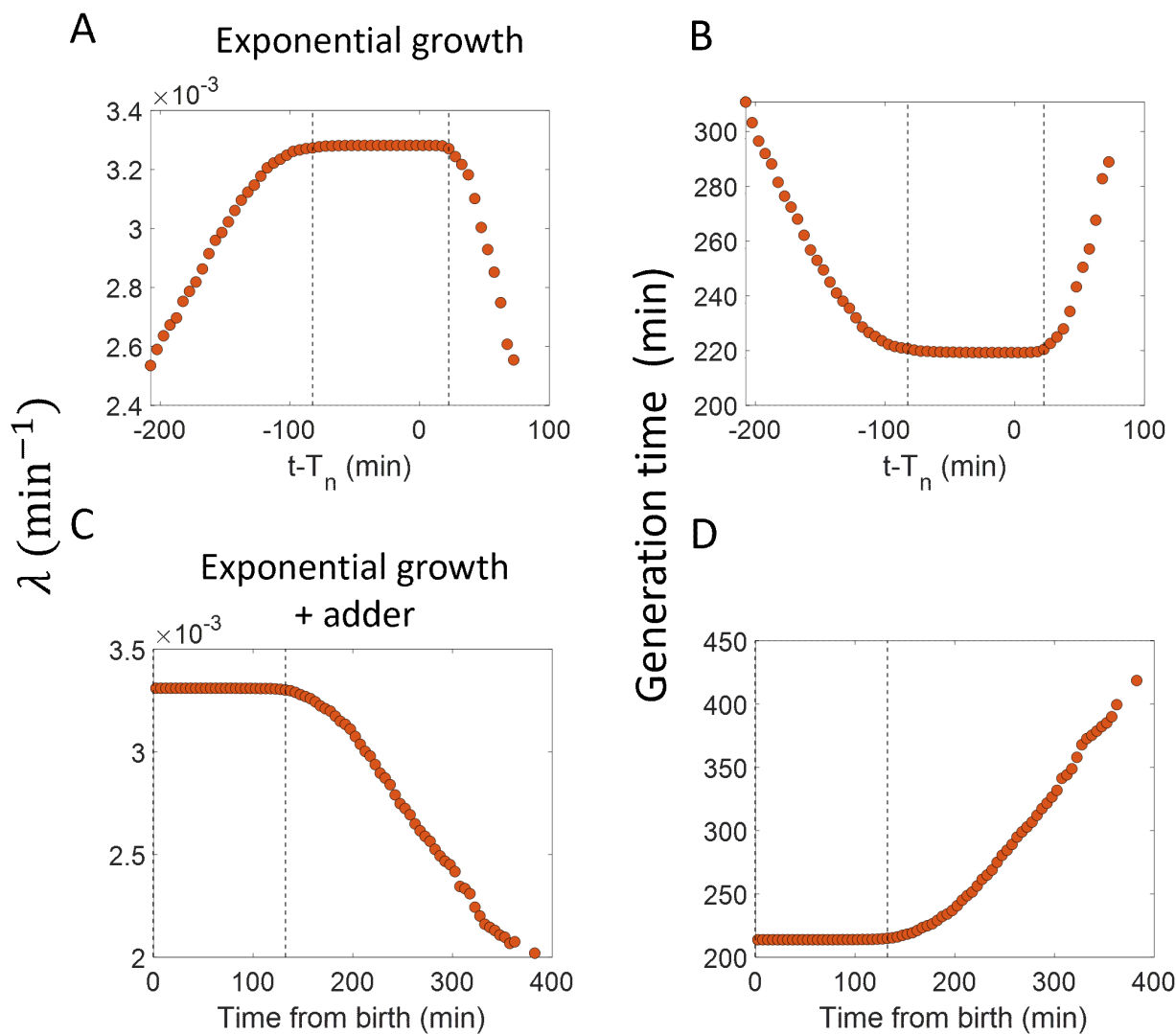
1107 Figure 2- figure supplement 1: **Experimental data:** $\ln(\frac{L_d}{L_b})$ vs $\langle \lambda \rangle T_d$ (left) and $\langle \lambda \rangle T_d$ vs
 1108 $\ln(\frac{L_d}{L_b})$ plot (right) is shown for, **A.** Cells growing in glycerol medium ($\langle T_d \rangle = 164$ min, $N =$
 1109 648 cells). **B.** Cells growing in glucose-cas medium ($\langle T_d \rangle = 65$ min, $N = 737$ cells). Binned
 1110 data (red), and the best linear fit (yellow) obtained by performing linear regression on the
 1111 raw data deviate from the $y=x$ line (black dashed line) in the case of $\ln(\frac{L_d}{L_b})$ vs $\langle \lambda \rangle T_d$ plots in
 1112 both media. However, both binned data and the best linear fit are in close agreement with
 1113 the $y=x$ line (black dashed line) on interchanging the axes. In all of these plots, the binned
 1114 data is shown only for those bins with more than 15 data points in them.



1116

1117 Figure 2- figure supplement 2: **Binned data trend in growth rate (λ) and inverse**
 1118 **generation time ($\frac{1}{T_d}$) plots:** **A-B.** Simulations of the adder model for exponentially
 1119 growing cells were carried out at multiple growth rates for $N = 2500$ cells. The size added
 1120 between birth and division and the mean growth rates were extracted from Kennard *et al.*,
 1121 [57]. The CV of growth rates was greater for cells growing in slower-growth media. See
 1122 Section 5.11.2 for the parameter values. For these simulations, we show **A.** λ vs $\frac{1}{T_d}$ plot. **B.**
 1123 $\frac{1}{T_d}$ vs λ plot. The smaller circles show the trend in binned data within a growth medium.
 1124 Different colors correspond to different growth media. Population means are shown as larger
 1125 markers. The population means agree with the expected $y = \ln(2)x$ line (black dashed line)
 1126 in Figure 2- figure supplement 2A but the trend within a single growth medium is non-linear
 1127 and deviates from the $y = \ln(2)x$ line. However, in Figure 2- figure supplement 2B, population
 1128 means across growth conditions and the trend in binned data within a single growth medium
 1129 follow the expected $y = \frac{1}{\ln(2)}x$ line (black dashed line).





1144

1145 Figure 3- figure supplement 2: **Inspection bias in the growth rate vs time plots**
 1146 **obtained from simulations:** **A.** The binned growth rate trend as a function of time
 1147 from the onset of constriction ($t-T_n$) is shown in red. Time $t-T_n = 0$ corresponds to onset of
 1148 constriction. The plot is shown for simulations of exponentially growing cells carried out over
 1149 $N = 2500$ cell cycles. Constriction length is determined by a constant length addition from
 1150 birth and division occurs after a constant length addition from constriction. **B.** The average
 1151 generation time for the cells present in each bin of Figure 3- figure supplement 2A is shown.
 1152 **C.** For simulations of exponentially growing cells following the adder model ($N=2500$), the
 1153 binned growth rate (in red) vs time from birth plot is shown. **D.** The average generation
 1154 time for the cells present in each bin of Figure 3- figure supplement 2C is shown. The vertical
 1155 dashed lines show the time range in which the generation times are approximately constant
 1156 and hence, the effects of inspection bias are negligible. Within that time range, the growth
 1157 rate trend is found to be constant, consistent with the assumption of exponential growth.

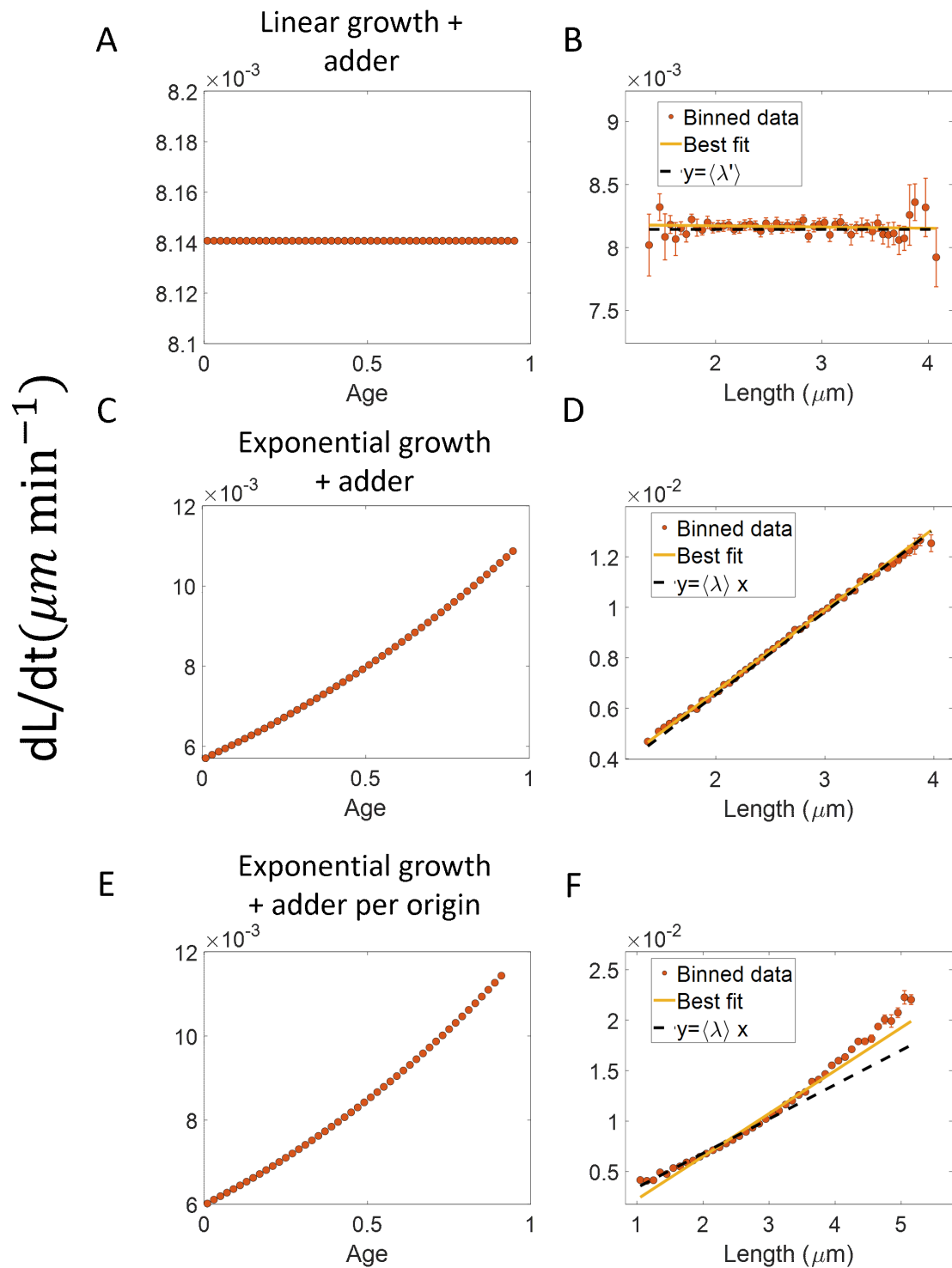
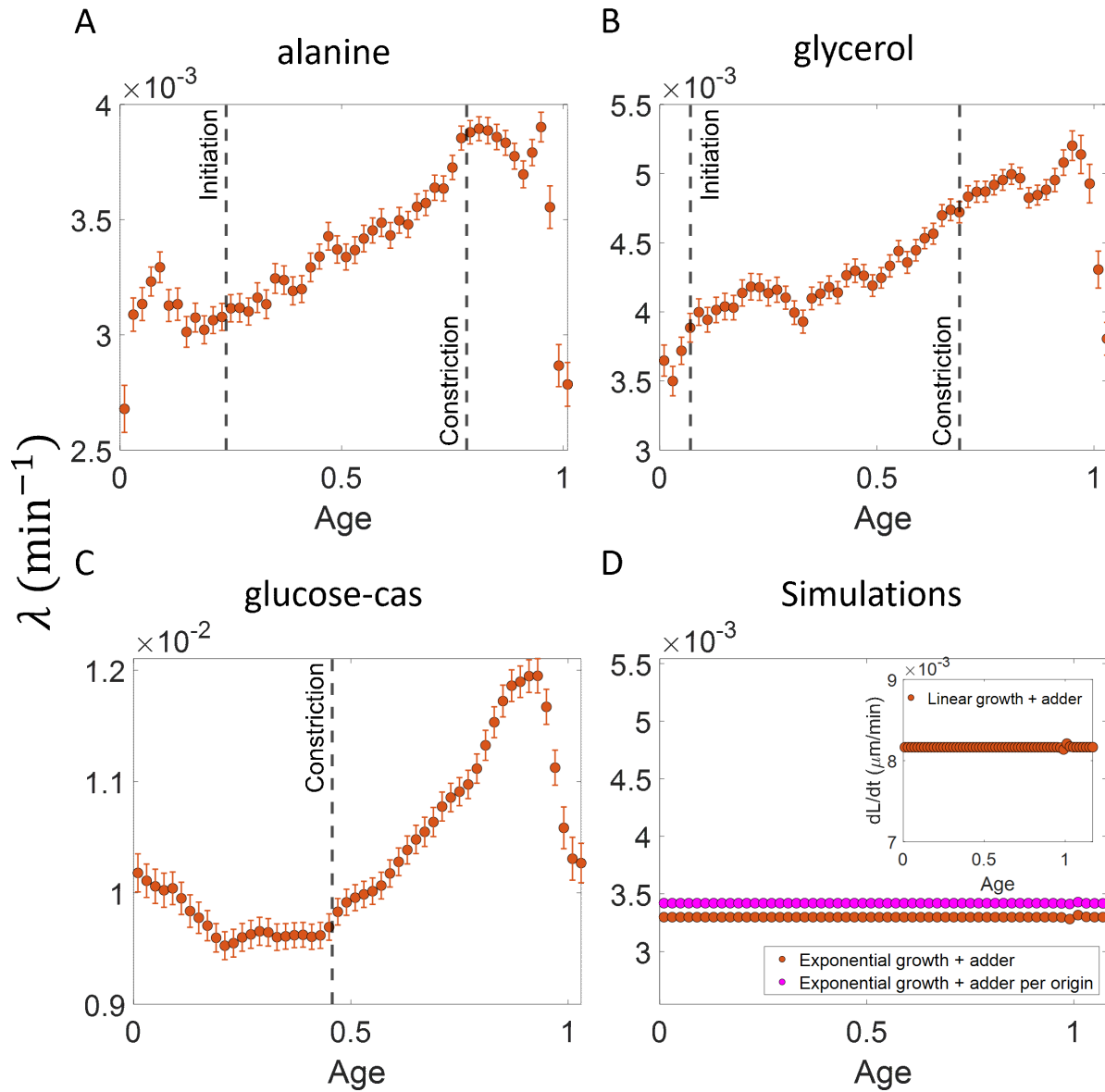


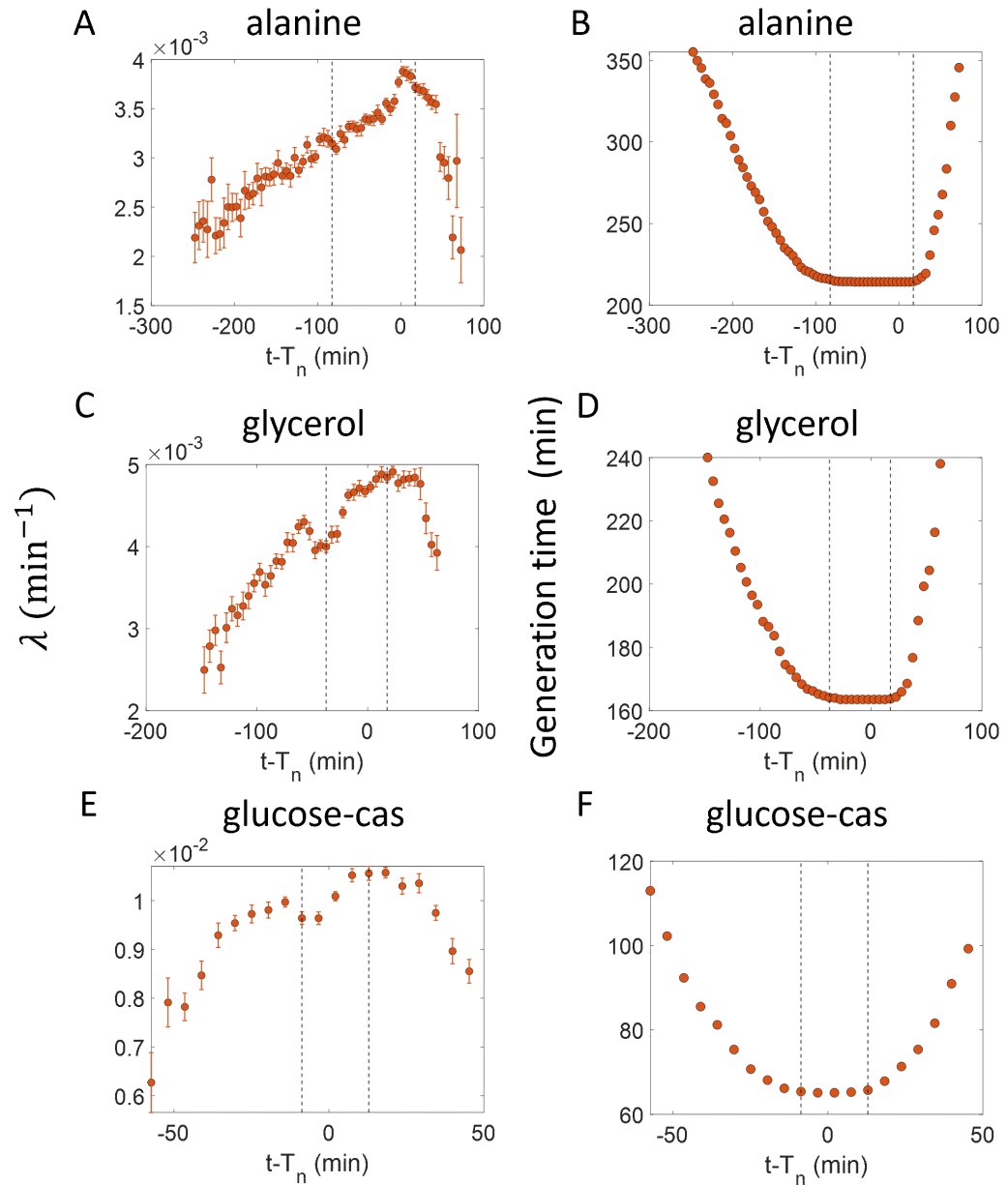
Figure 3- figure supplement 3: **Differential methods of quantifying growth: A-B.** Simulations of linearly growing cells following the adder model are carried out for $N = 2500$ cell cycles. Cell size (L) data is recorded as a function of time within the cell cycle. **A.** The red dots show the binned data for elongation speed as a function of age. The trend is almost constant in agreement with the linear growth assumption. **B.** Elongation speed is also constant with cell size as expected for linear growth with the intercept value being the average elongation speed. **C-D.** Simulations of exponentially growing cells following the adder model are carried out for $N = 2500$ cell cycles. **C.** Elongation speed trend (in red) increases with age in agreement with the exponential growth assumption. **D.** Elongation speed trend (in red) increases linearly with size with a slope equal to the average growth rate. **E-F.** Simulations of exponentially growing cells following the adder per origin model are carried out for $N = 2500$ cell cycles. **E.** Again, the elongation speed trend (in red) increases with age in agreement with the exponential growth assumption. **F.** Elongation speed trend (in red) deviates from the expected linear trend (black dashed line). This could be misinterpreted as non-exponential growth. Thus, we find that the binned data trend for the plot elongation speed vs size is model-dependent.



1160

1161

Figure 4- figure supplement 1: **Growth rate vs age curves extended beyond the division event: A,B,C.** The binned growth rate trend is shown in red as a function of age for *E. coli* experimental data. The trends are obtained using the cell size trajectories extending beyond the division event (age>1). The plots are shown for **A.** Alanine medium (N = 720 cells) **B.** Glycerol medium (N = 594 cells). **C.** Glucose-cas medium (N = 664 cells). The error bars in all three plots represent the standard deviation of the growth rate in each bin scaled by $\frac{1}{\sqrt{N}}$, where N is the number of cells in that bin. The growth rate trend appears to be periodic in each of the growth media i.e., λ at age ≈ 1 is close to λ at age ≈ 0 . These trends agree with that of Figure 4 in the appropriate age ranges. **D.** Simulations are carried out for N= 2500 cell cycles. The cell size trajectories are collected beyond the division event (age>1). The binned data trend for growth rate vs age plot is shown in red for exponentially growing cells following the adder model. We observe the trend to be nearly constant as expected for exponential growth. The binned growth rate trend is also found to be nearly constant for the simulations of exponential growing cells following the adder per origin model (shown in magenta). (Inset) Shown in red is the elongation speed vs age plot for simulations of N= 2500 cell cycles of linearly growing cells following the adder model. As expected for linear growth, the binned elongation speed trend remains approximately constant with age. The growth rate trends for the models with exponential growth agree with that of Figure 3B. The elongation speed trend (inset) also agrees with the trend in Figure 3- figure supplement 3A.



1162

Figure 4- figure supplement 2: **Inspection bias in the growth rate vs time from constriction plots obtained from experiments: A,C,E.** The binned growth rate trend is shown in red as a function of time from the onset of constriction ($t-T_n$). Time $t-T_n = 0$ corresponds to the onset of constriction for all cells considered. The plots are shown for **A**. Alanine medium. **C**. Glycerol medium. **E**. Glucose-cas medium. The error bars in all three plots represent the standard deviation of the growth rate in each bin scaled by $\frac{1}{\sqrt{N}}$, where N is the number of cells in that bin. **B,D,F**. The average generation time for the cells present in each bin of **B**. Alanine medium (Figure 4- figure supplement 2A) **D**. Glycerol medium (Figure 4- figure supplement 2C) **F**. Glucose-cas medium (Figure 4- figure supplement 2E) are shown. The vertical dashed lines represent the time range within which the average generation time remains approximately constant. The growth rate trends within this time range are consistent with that in Figure 4 for the respective growth condition as there is negligible inspection bias.